TESTING COSMOLOGICAL MODELS BY GRAVITATIONAL LENSING. I. METHOD AND FIRST APPLICATIONS

JOACHIM WAMBSGANSS

Astrophysikalisches Institut Potsdam, 14482 Potsdam, Germany; jwambsganss@aip.de

AND

RENYUE CEN AND JEREMIAH P. OSTRIKER

Princeton University Observatory, Princeton, NJ 08544; cen@astro.princeton.edu, jpo@astro.princeton.edu

ABSTRACT

Gravitational lensing directly measures mass density fluctuations along the lines of sight to very distant objects. No assumptions need to be made concerning bias, the ratio of fluctuations in galaxy density to mass density. Hence, lensing is a very useful tool for studying the universe at low to moderate redshifts.

We describe in detail a new method for tracing light rays from redshift zero through a three-dimensional mass distribution to high redshift. As an example, this method is applied here to a standard cold dark matter universe. We obtain a variety of results, some of them statistical in nature, others from rather detailed case studies of individual lines of sight. Among the statistical results are the frequency of multiply imaged quasars, the distribution of separation of multiple quasars, and the redshift distribution of lenses, all as functions of quasar redshift. We find effects ranging from very weak lensing to highly magnified multiple images of high-redshift objects, which for extended background sources (i.e., galaxies) range from slight deformation of shape to tangentially aligned arclets to giant luminous arcs.

Different cosmological models differ increasingly with redshift in their predictions of mass (and thus gravitational potential) distributions. Our ultimate goal is to apply this method to a number of cosmogonic models and to eliminate some models for which the gravitational lensing properties are inconsistent with those observed.

Subject headings: cosmology: theory — gravitational lensing — methods: numerical

1. INTRODUCTION

Each specific model for the development of cosmogonic structure (e.g., the hot dark matter [HDM] or cold dark matter [CDM] scenarios) has one free parameter, the amplitude of the density power spectrum. In light of *COBE* observations (Smoot et al. 1992; Górski et al. 1994), for the first time this parameter has been fixed ($\pm 12\%$) by determination on the $5°$–$10°$ scale in the linear regime. With its amplitude fixed, a secure determination of the potential fluctuation on any other scale provides a test for any particular cosmological model. Any single conflict between the theory and reality can falsify the theory. The most leverage is obtained for tests that are made on angular scales as far away as possible from the *COBE* measurements. But they should not be so small as to be greatly influenced by the difficulty inherent in modeling the physics of gaseous, baryonic components (≤ 10 kpc). Thus, critical tests are best made on scales of 0.01 Mpc $< r < 1$ Mpc. Gravitational lensing *directly* measures the fluctuations in the gravitational potential along random lines of sight to distant objects. In contrast, the conventional tools for comparing cosmogonic theories with observations rely on either galaxy density or galaxy velocity information, both of which unavoidably suffer from uncertainties with regard to the density or velocity bias of galaxies over the underlying mass distribution, hampering our attempts to understand the more fundamental questions concerning mass evolution and distribution. Hence, gravitational lensing provides a powerful independent test of cosmogonic models because of its unique ability to directly measure the gravitational

potential fluctuations. The sampled properties of cosmic structure on certain scales are also more "fair" than other conventional measures owing to the fact that lines of sight to distant objects are *random* with regard to the foreground matter distribution.

We present here a method for determining gravitational lensing effects for realistic mass distributions from the weak to the strong lensing regime. First, we fill the universe "densely" with adjacent mass cubes, taken from cosmological simulations, along the line of sight; inside each cube, the matter is projected onto the middle plane. We then study the lensing properties of the intervening matter by "shooting" light rays through the lens (mass) planes representing matter distributions along redshifts (see Fig. 1 for a schematic version of our actual plan, which uses on the order of 100 lens planes). The gravitational lens effects of many lens planes have been studied by several authors in the past (e.g., Kochanek & Apostolakis 1988; Schneider & Weiss 1988a, 1988b; Jaroszyński 1989, 1991; Jaroszyński et al. 1990; Lee & Paczyński 1990; Babul & Lee 1991; Bartelmann & Schneider 1991). These authors typically used point lenses or isothermal spheres randomly distributed on individual lens planes. The number of lens planes used ranges from two to 32. Most of these studies involved the regime of weak lensing, i.e., slight effects on the magnification of sources but not multiple imaging. Rauch (1991) studied the microlensing effect of three-dimensionally distributed point lenses on high-redshift supernovae. A complementary approach to the one described here, a semianalytical method using the Press-Schechter formal-
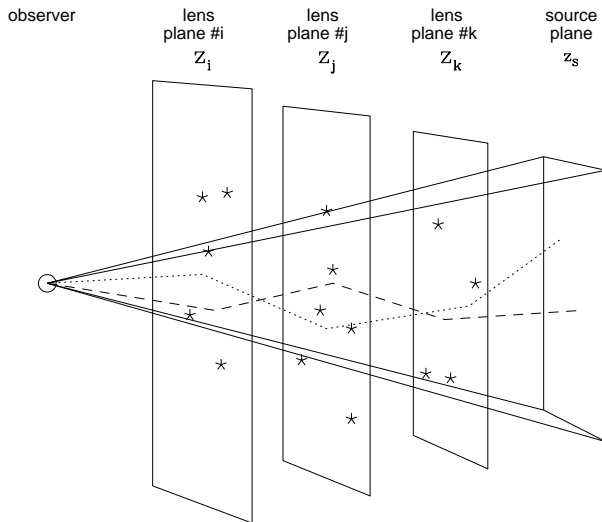
FIG. 1.—Schematic depiction of the bundle of light rays with fixed opening angle traversing many planes with constant comoving (but increasing physical) side length. For simplicity, we show only three lens planes; in fact, we use on the order of 100 individual planes. The observer is at the left, the source plane is at the right. Redshifts of the lens planes are increasing from left to right (i.e., $0 < z_i < z_j < z_k < z_S$). The bundle of light rays "illuminates" a small fraction of the lens planes at low redshift. This fraction increases with redshift to almost 1 at the highest lens redshift.

ism, was first used by Narayan & White (1987), and more recently applied by Kochanek (1995) to various cosmological models.

A very preliminary attack on the problem of studying the lensing properties of different cosmological models has been presented by Cen et al. (1994, hereafter CGOT). In that work, no ray tracing was done. Rather, they simply checked whether or not mass accumulations were greater than the critical level at which multiple imaging will occur (cf. Turner, Ostriker, & Gott 1984, henceforth TOG). The mathematical and physical treatment here is far superior to that adopted in CGOT; the essential conclusions for the standard CDM scenario, however, are unchanged. Some of these conclusions have already been presented in Wambsganss et al. (1995). Here we provide the mathematical basis of that method as well as some tests of the method.

We use cosmological simulations for the standard *COBE*-normalized $\Omega = 1$, CDM universe as an example to illustrate the method. A first report on the results has been published elsewhere (Wambsganss et al. 1995). Mass distributions from many different cosmological models will be treated with this method. The ultimate goal of this project is to provide a quantitative comparison of the lensing properties of different cosmological models (e.g., CDM with $\Omega = 1$, low-density (open) CDM models, mixed dark matter [MDM] models, flat models with a cosmological constant, isocurvature models, etc.) with observations. For example, we anticipate that different cosmological models, which are typically tuned to give approximately correct properties when compared with our local universe at redshift $z = 0$, will show different lensing properties, because they reach the final state ($z = 0$) from quite different paths. Thus, the typical lens will appear at different redshifts in different models. For example, in MDM models, where structure forms late, the lenses will have small redshift; but in isocurvature models, where the first structures form shortly after recombination, the average lens redshift will be much larger.

For many questions (e.g., the fraction of multiply imaged quasars as a function of angular separation, magnification ratio, or redshift) one needs a large number of simulations with different realizations of the matter distribution in order to give quantitative answers on a good statistical basis. For other applications, such as detailed studies of lensing by clusters of galaxies and the effects of chance alignments with foreground or background matter, a specific realization must be studied in detail.

While in principle it is possible to numerically simulate in one model the entire path from observer to source (very large simulations with elongated geometry have been done; e.g., Park & Gott 1991), technical limitations preclude this at present. For now, we perform many independent simulations for different volumes along the line of sight (since repeated structures are obviously to be avoided). We have developed an approximate technique for this, which we term the "convolution method." Physically, it consists of assuming that separate pieces of an inhomogeneous universe act as if they were part of an homogeneous universe of the same mean density as themselves. Details of the method, which is an improved version of that applied in CGOT, are presented in the Appendix, together with detailed checks that indicate the accuracy of the approximations involved.

Although we think that this convolution technique describes the properties accurately enough on the scales of interest to us, we hope in future to be able to avoid this step and use simulations that have a large enough dynamic range to cover a representative part of the universe and high enough resolution to represent the potential wells of galaxies, groups, and clusters appropriately. The analytical techniques presented in this paper for determining lens properties are independent of the details of the method for computing the evolution. We will use the same ray tracing method when we later utilize higher resolution numerical evolution techniques that do not depend on the convolution method.

The rest of the paper is organized as follows. The ray-shooting technique is described and discussed in detail in § 2. As a result of this ray shooting, we obtain a mapping of the rays from the image plane (sky plane) to the source plane. With this mapping, we determine the magnification distribution of background sources, the fraction of the source plane that is multiply imaged, and the positions and shapes as well as the topology of the caustics and the corresponding critical lines (§ 3). For a set of given source positions and shapes in the source plane at a given redshift, we determine and analyze the corresponding image configurations as they would appear in the sky, as is shown in §§ 4 and 5. Finally, in § 6 we give a short summary and describe the planned applications and the types of predictions we will be able to make for different cosmological models.

2. MULTIPLANE LENS EQUATION, RAY SHOOTING, AND TESTS

In Schneider, Ehlers, & Falco (1992, hereafter SEF) an entire chapter deals with the theory of multiple light deflection, i.e., gravitational lensing by more than one plane. We refer the interested reader to that text for details. Here we simply describe the multiplane lens equation as we use it:

$$\binom{y_1}{y_2} = y = x - \sum_{i=1}^{N} \frac{D_{is}}{D_s} \alpha_i(x)$$

$$= \begin{bmatrix} a_{11}(x) & a_{21}(x) \\ a_{12}(x) & a_{22}(x) \end{bmatrix} \binom{x_1}{x_2} = A(x)x . \quad (1)$$

Here, x is the position vector of a light ray in the first lens plane (or, equivalently, in the image/sky plane), y is its corresponding position in the source plane, α_i is the (two-dimensional) deflection angle in the lens plane i, and D_s and D_{is} are the angular diameter distances between observer and source plane and between the ith lens plane and source plane, respectively. The lens planes are labelled 1 through N in order of increasing redshift.

The part of the equation that we are essentially interested in is $y = A(x)x$, which describes the mapping between the image/sky plane and the source plane. The relation between the positions x in the image/sky plane and y in the source plane is given by $A(x)$, the Jacobian matrix of the mapping. In the case of multiple lens planes, the Jacobian

$$A(x) \equiv \frac{\partial y}{\partial x} , \quad A_{ij} \equiv \frac{\partial y_i}{\partial x_j} \quad (2)$$

does not have all the nice properties it has in the single lens plane case; in particular, it is no longer symmetric in the general case: $a_{12} \neq a_{21}$. Furthermore, it is not curl free: curl $A \neq 0$. Many other properties, however, are still valid. The magnification of a certain image at position x is given as

$$\mu(x) = [\det A(x)]^{-1} = [a_{11}(x)a_{22}(x) - a_{12}(x)a_{21}(x)]^{-1} . \quad (3)$$

Other combinations of the components of det $A(x)$ represent useful quantities as well. The effective surface mass density κ (basically the sum of the physical surface mass densities of the individual lens planes weighted by the corresponding ratios between the angular diameter distances) for any position x in the sky plane is given as

$$\kappa(x) = 1 - 0.5[a_{11}(x) + a_{22}(x)] . \quad (4)$$

Similarly, the components of the shear $\gamma(x) = [\gamma_1(x), \gamma_2(x)]$ are

$$\gamma_1(x) = -0.5[a_{11}(x) - a_{22}(x)] , \quad (5a)$$

$$\gamma_2(x) = -0.5[a_{12}(x) + a_{21}(x)] . \quad (5b)$$

In order to "shoot" a light ray i through a single lens plane, one must determine the deflection angle α_i of this ray due to all matter in this lens plane. For a number of n point lenses, this is simply a summation of the deflection angle by each point lens j:

$$\alpha_i = \sum_{j=1}^{n} \alpha_{ji} = \frac{4G}{c^2} \sum_{j=1}^{n} M_j \frac{r_{ij}}{r_{ij}^2} . \quad (6)$$

Here, G and c are the gravitational constant and the speed of light, respectively, M_j is the mass of point lens j, r_{ij} is the projected (vector) distance between the positions of light ray i and point lens j, and r_{ij} is its absolute value, $r_{ij} = [(x_i - x_j)^2 + (y_i - y_j)^2]^{1/2}$, with (x_i, y_i) being the position of ray i and (x_j, y_j) the position of lens j.

The straightforward determination of one deflection angle takes about ten floating point operations. As a lens plane, we consider a two-dimensional distribution of matter

given in a grid; for the examples here, we always use a regular matter grid with 500×500 positions (in subsequent work we will increase the resolution to 800×800 positions; in principle, this can be increased to any desired resolution, depending on the desired purpose). This is the projection of the three-dimensional matter distribution inside a cube with comoving side length $L = 5 \, h^{-1}$ Mpc (where $h = H_0/100$ is the Hubble constant divided by 100) onto one of the three faces of the cube. We treat this matter distribution as 250,000 point lenses, or more accurately as "smeared out" in matter or lens pixels in a square region of comoving 10 h^{-1} kpc at a side. We must determine the deflection angle for at least as many positions as there are lens pixels, i.e., on at least a 500×500 grid (again, this is the resolution we use for the examples here, which can be changed to whatever ray density is appropriate to the problem at hand). Because we use on the order of 100 lens planes, the total number of mathematical operations for a direct determination of the deflection angle amounts to about $10 \times 500^2 \times 500^2 \times 100 \approx O(10^{14})$ floating point operations. This is nontrivial, even for fast computers.

In order to speed up the calculation, we determine the deflection angle in each lens plane with a hierarchical tree code in two dimensions, as described in Wambsganss (1990). The idea is to group together lenses that are far away from the light ray, and treat these "cells" (whose sizes increase with distance to the ray) as pseudo lenses. Nearby lenses are treated individually, lenses at intermediate distances to the light ray are grouped into small cells of a few lenses, and lenses very far away from the light ray considered are grouped into cells containing up to a few thousand lenses. This tree code treatment speeds up the determination of the deflection angle by a large factor. The number of lenses and pseudo lenses necessary for an accurate determination of the deflection angle in one plane is on the order of 100 (rather than the 250,000 needed for the direct determination). There is some overhead, namely in the determination of the tree structure for each ray, i.e., the determination of which lenses are to be treated directly and which are to be put into cells of different sizes. However, this is done just once, and the configuration used again in all subsequent planes, since the relative positions of the lenses are exactly the same. The cost of this additional calculation is negligible compared to that of a direct determination of the deflection angles.

In its simplest application, the tree code assumes that all matter inside a cell is located at its center of mass. However, we use higher order multipoles of the mass distribution in order to increase the accuracy (cf. Wambsganss 1990). For the actual calculations, we use multipoles of up to order 6. In Figure 2, we show the deviation of the deflection angle determined with this tree-code method from the directly determined (i.e., accurate) deflection angle, $\alpha_{\text{direct}} - \alpha_{\text{tree}}$, as a function of α_{direct} in arbitrary units (top row indicates the x-component, bottom row the y-component). The panels correspond to determinations of α_{tree} that include multipoles of different orders, representing (1) all matter in center of mass, i.e., only the monopole term (leftmost column), (2) monopole term plus quadrupole moments (second column), (3) monopole term plus all multipoles up to order 4 (third column), and (4) monopole term plus all multipoles up to order 6 (rightmost column). In the actual calculation of the deflection angle we use multipoles of up to order 6, corresponding to the rightmost panel. It can be seen that for this
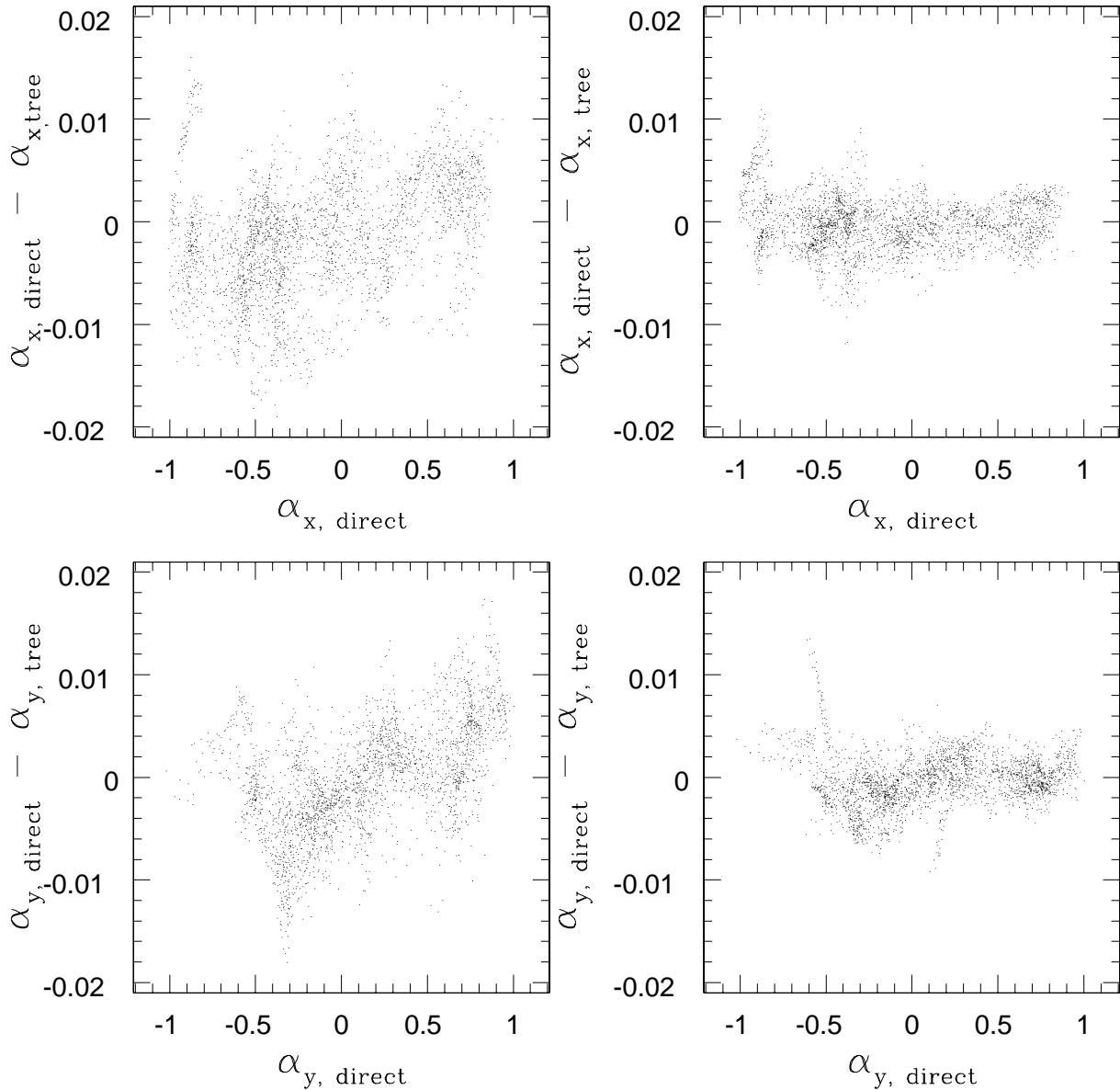
FIG. 2.—Displayed is the effect of increasing the accuracy of the hierarchical tree code for the determination of the deflection angle by using multipoles of higher order. The top row treats the x-component and the bottom row the y-component of the deflection angle. The difference between direct determination and tree-code determination is shown vs. the direct determination (in arbitrary units). In the leftmost column, the tree code uses only the monopole term, i.e., it assumes all the matter is at the location of the center of mass of each cell. The accuracy of the angle determination in this case is about 1%. In the next columns, the same is shown for a tree code including quadrupole moment (*second column*) and tree code with all moments up to order 4 (*third column*). In the rightmost column, all multipole moments up to order 6 are included in the determination of the deflection angle. The maximum deviation in the last panel is clearly better than 0.1%. All our lensing calculations are done with this accuracy.

case, the largest fractional deviation between the two methods of determining the deflection angle is on the order of 2×10^{-3}, with the rms deviation quite a bit smaller. This seems to be a good enough approximation for our purposes.

For point lenses, the deflection angle formally diverges when the distance between light ray and lens position becomes zero, $r_{ij} \rightarrow 0$. However, in our case, this is an artificial divergence; since the underlying mass distribution is smooth, we only approximate it by a large number of point lenses. In order to avoid this artificial divergence, we always determine the deflection angle at the points directly in the center of four lens positions, so that nearest neighbor effects cancel. That means that for each lens plane we determine the deflection angles for a regular grid of "test rays." But

since the real positions of the light rays are offset from the positions of the test rays for which we determined the deflection angles, we calculate the actual deflection angles of the rays that are followed through the planes using a bicubic interpolation among the four test rays surrounding the real ray position. In this way, we obtain a smooth two-dimensional field of deflection angles for each lens plane, as is to be expected for a continuous matter distribution.

The angular size of the (square) bundle of light rays that we consider is determined by the angular size of the highest redshift lens plane that we use. For example, the angular size of a cube with comoving size $L = 5 \ h^{-1}$ Mpc at a redshift $z = 3$ is about $\beta \approx 350''$ for a standard CDM universe. The (average) angular size of the field of rays is fixed, and is the same for all lens planes; however, as the physical
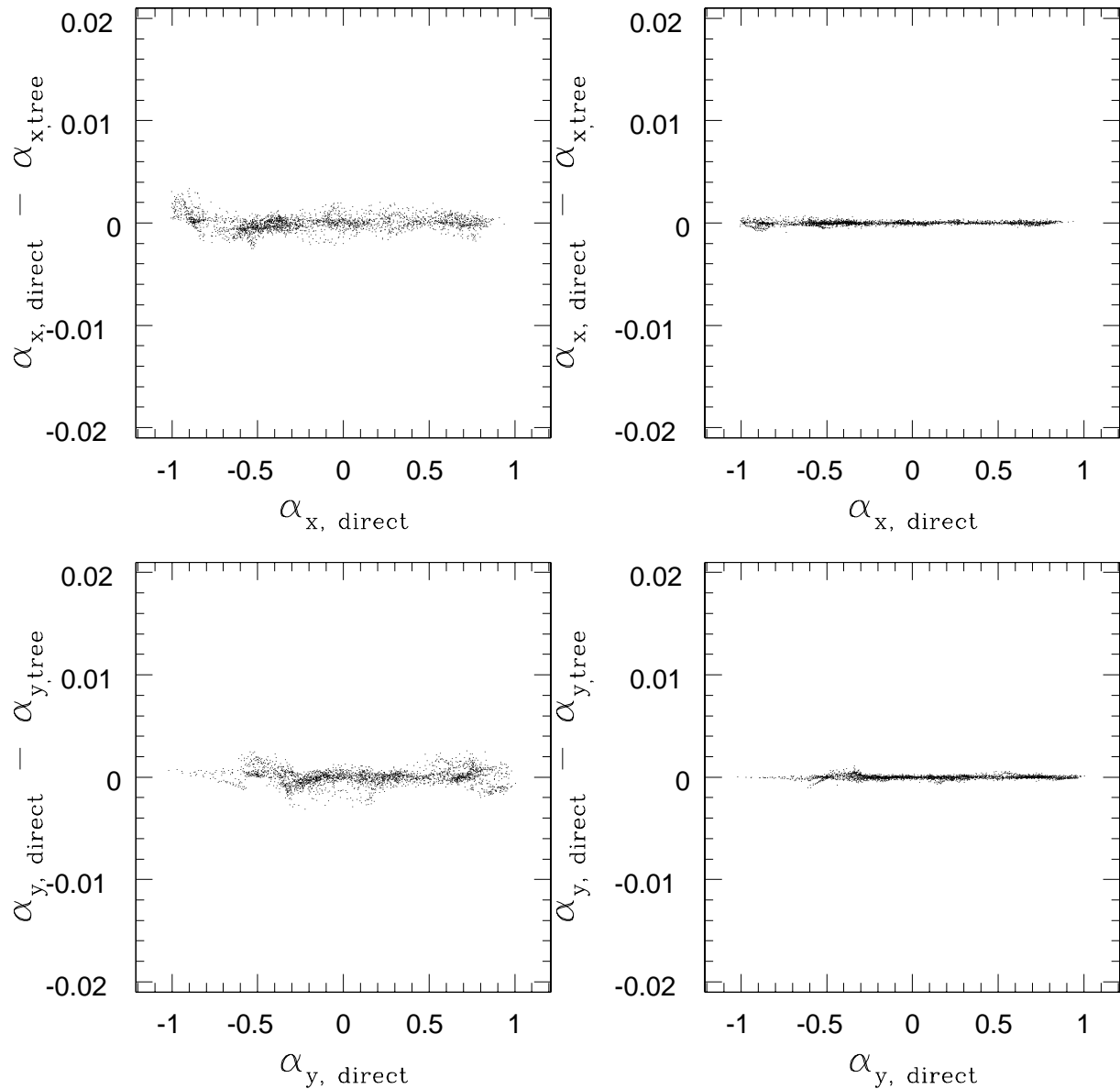
FIG. 2—Continued

size of the underlying cosmological cubes is expanding with decreasing redshift, the angular size of the lens planes increases rapidly with decreasing redshift. This means that the field of real rays intercepts only a small part of the lens plane for small redshifts (cf. Fig. 1). This effect is reflected in the matter distribution inside the field of view; for low redshift lens planes, one lens pixel (with a fixed comoving size) covers quite a large angular region.

The matter distribution of each lens plane inside the field of rays is shown in Figure 3a for a particular line of sight; dark gray means high and light gray means low surface mass density (in g cm^{-2}). From top left to bottom right, we see the matter inside the beam for 60 different lens redshifts, starting with $z \approx 0$ and increasing to $z \approx 3.0$. For the low-redshift planes, one can easily identify the pixel size of the matter distribution, because one matter pixel [physical size $5\,h^{-1}\,\mathrm{Mpc}/(1+z)/500 = 10\,h^{-1}(1+z)^{-1}\,\mathrm{kpc}$] corresponds to many tens of arcsecsonds. In Figure 3b, the integrated matter distribution up to a redshift $z \approx 3.0$ is shown. This is

the "physical" sum, i.e., in units of mass per physical area. This map could be converted into a map of light if one assumes, e.g., a constant mass-to-light ratio and weights the individual lens planes by the inverse of the (luminosity) distance. If one compares Figures 3a and 3b, it is quite obvious that the total surface mass density is dominated by a few planes along the line of sight. In general, lensing is a very convergent process; it is not a result of the sum of a large number of weak lensing events, but rather is due to the occasional passage of a light ray past a large mass concentration. This fact makes the requirements for statistical validation of our results especially stringent. Many independent realizations of the universe must be made and many lines of sight examined before one can have confidence (by examination of convergence) that the derived statistical results are robust (i.e., that the statistically averaged results become independent of the number of realizations studied).

For each lens plane, the critical surface mass density, Σ_{crit}, necessary for multiple imaging is calculated as
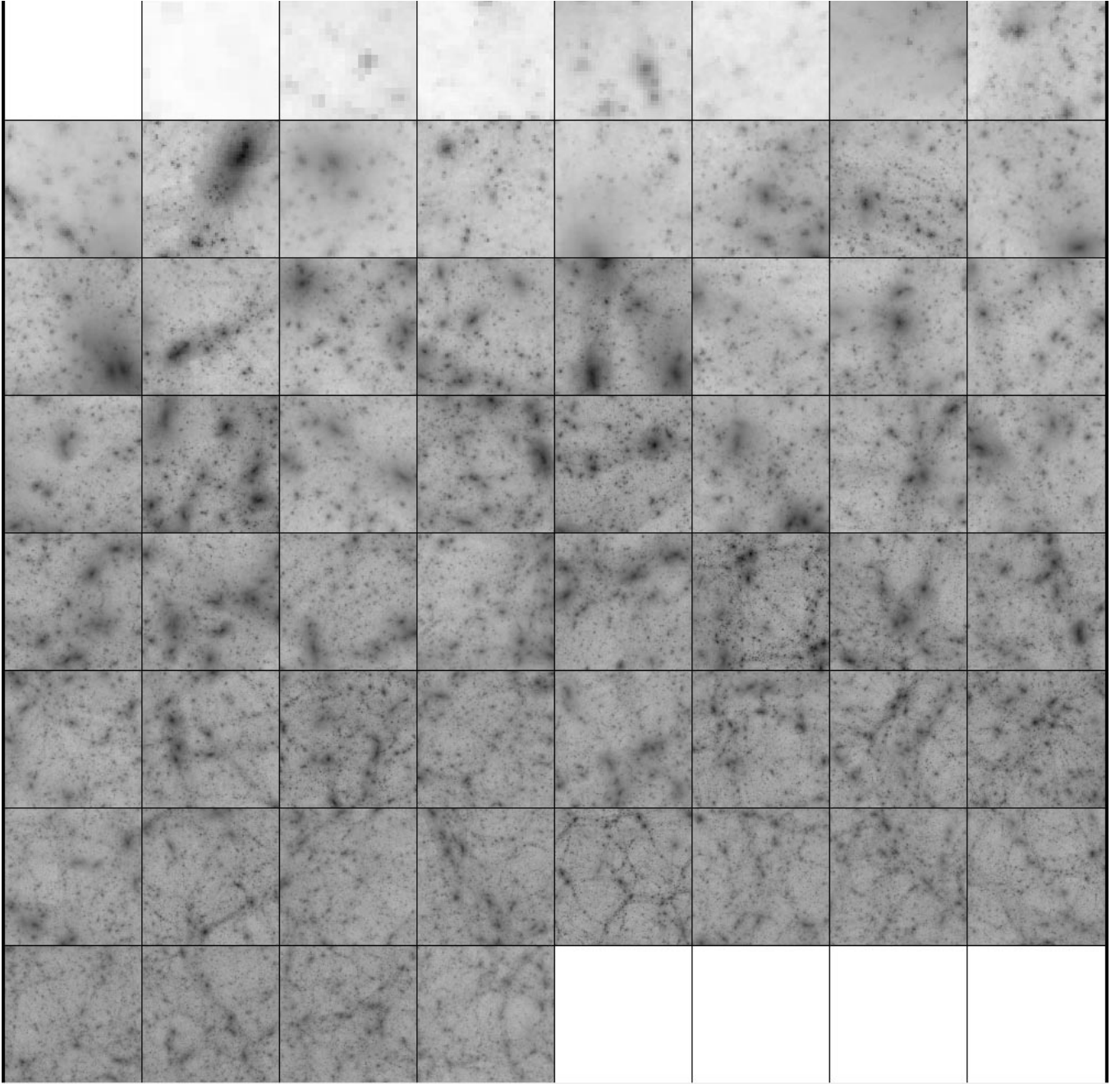
FIG. 3a

FIG. 3.—The matter distribution in physical units (g cm^{-2}) inside the beam of rays is shown. Dark shading indicates high values of the surface mass density. (a) 60 panels contain the matter distribution of individually treated lens planes. The "first" plane is top left (lowest redshift), with redshift increasing to the right. The highest redshift plane is the last section in the bottom row at $z = 3$. In (b), this matter is displayed integrated along the line of sight up to a redshift of $z = 3$.

(cf. SEF)

$$\Sigma_{\rm crit} = \frac{c^2}{4\pi G} \frac{D_s}{D_i D_{is}} . \qquad (7)$$

Comparing the surface mass density in each matter pixel (m, n) with this value identifies the regions that should produce multiple images of a background source:

$$\kappa_{m,n} = \frac{\Sigma_{m,n}}{\Sigma_{\rm crit}} = \Sigma_{m,n} * \frac{4\pi G}{c^2} \frac{D_i D_{is}}{D_s} ,$$

where $\Sigma_{m,n}$ is the physical surface mass density in pixel (m, n), and $\kappa_{m,n}$ is its normalized surface mass density. When $\kappa_{m,n} > 1$, multiple lensing occurs. We note that overdensity in a single plane is a sufficient but not a necessary condition of multiple imaging; chance alignments of two or more individually subcritical but collectively supercritical regions can produce multiple images as well as slightly underdense regions in combination with a sufficiently large shear. A comparison of such regions with the actual location of multiple images found by the ray shooting serves as a good check of the whole method.
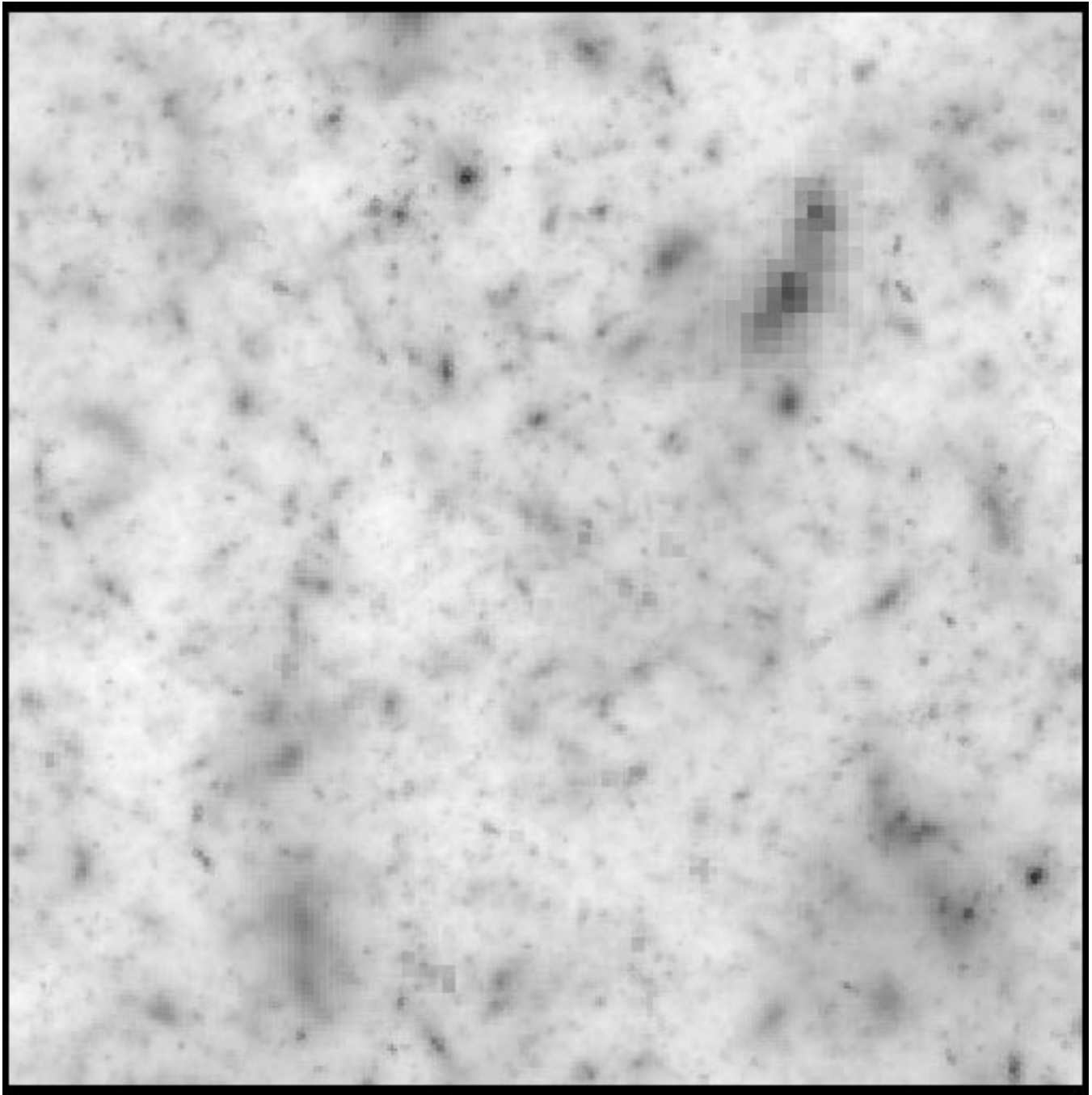
FIG. 3b

For each complete run of the light rays through all the lens planes, the positions of the light rays in the image/sky plane and the corresponding positions in the source plane are stored. In subsequent sections we describe how the matter distribution is obtained in each lens plane and how the mapping of light rays through an essentially realistic three-dimensional matter distribution is analyzed. But first, we would like to add a few paragraphs discussing the issue of numerical resolution and describing an additional test of our method.

Many authors have studied magnification cross sections and caustic structures of various lens models. To name just a few, Blandford & Kochanek (1987) and Kochanek & Blandford (1987) studied magnification cross sections and probability distributions for isolated elliptical potentials; Hinshaw & Krauss (1987) determined the lensing probabilities for isothermal spheres with finite cores; Wallington & Narayan (1993) investigated the influence of the core radius on the imaging properties of elliptical lenses; Kovner (1987a, 1987b) looked into "marginal" lenses; and Kassiola & Kovner (1993) compared the lensing properties of elliptical mass distributions with elliptical potentials. Most of these authors studied idealized lens models in great detail. In order to get a good representation of, e.g., the magnification probability of a certain elliptical lens, one needs a grid of rays with good coverage of the source plane, in particular of the multiply imaged region (on the order of 1000×1000 rays).

We have a very different objective here. We study large-scale statistical lensing properties of the matter rather than modeling individual lenses in great detail. Therefore, our resolution requirements are very different from the examples mentioned above; we have many fewer rays covering the caustics region of our multiply imaging lenses. This is because of the different questions we try to answer. Nevertheless, we would like to know how well the lensing properties are reproduced in the high-magnification regions. Therefore, we compare the lensing properties of ideal elliptical lenses obtained with our method to the high-resolution results obtained by others.

First, we will briefly describe our method for determining the magnification. We evaluate the magnification in a regular grid in the source plane, as is explained in more detail in § 4. This is done by using the differential deflection properties of the four rays closest to the grid position to be evaluated. Subsequently, we interpolate two-dimensionally to determine the magnification value at the desired position in the source plane. In this way we do get a moderate resolution, although certainly not a perfect coverage of the multiply imaged region; a region with a size of about $350'' \times 350''$ is covered by about 500×500 resolution elements in the examples here. However, we emphasize again that the resolution is not hardwired in this method.

Below, we present a test for the accuracy of the magnification distribution obtained by our method, using elliptical lenses. We run examples with a single lens plane populated by an isolated elliptical lens with various values of ellipticity, velocity dispersion, and core radius, as described by Wallington & Narayan (1993, hereafter WN93). The results of these tests show that the qualitative lensing properties (the caustic geometry and the evolution of the caustic/critical line structure with increasing core radius, as shown in Fig. 1 of WN93) are well reproduced.

We also did a detailed quantitative comparison of the magnification distributions produced by the various elliptical lenses with the cross sections presented by WN93 (see their Fig. 3). We determined the cross sections for lensing of elliptical lenses with nine different velocity dispersions ranging from $\sigma_v = 370$ km s^{-1} to 1000 km s^{-1}. Ellipticities were chosen between 0.0 and 0.2, and we varied the core radii from 10% to 100% of the Einstein radius of a corresponding circular symmetric isothermal sphere. We compared the cross sections for magnifications larger than 2, 4, 8, 16, 32, ... with the values obtained by WN93. For each lens, as specified by the parameter set of velocity dispersion, ellipticity, and core radius, we run 10 different realizations (of angle relative to the coordinate axes and position of the center of the lens). We here summarize the comparison of our results with those of WN93 for three values of the velocity dispersion, $\sigma_{v1} = 370$ km s^{-1}, $\sigma_{v2} = 630$ km s^{-1}, and $\sigma_{v3} = 1000$ km s^{-1}, all with ellipticity $\epsilon = 0.2$, and with various core radii. The distributions $\sigma(>\mu)$ for magnifications $\mu = 2$, 4, and 8 agreed within about 15% or better for all three values of σ_v. For $\mu = 16$, the deviations were still moderate for the two higher σ_v-values (23% and 11%), while it was worse for the low velocity dispersion σ_{v1}. Even for $\mu = 32$, the deviation was only 30% for σ_{v3}, but quite large for the two lower values.

These results indicate that the cross sections of gravitational lenses with velocity dispersions at or below 1000 km s^{-1} are relatively well represented in the low and intermediate magnification regime. At high magnifications they are not very accurately represented in our simulations with the given resolution. However, the fluctuations in the cross sections are mostly of a statistical nature (the high-magnification regions are covered by only a small number of resolution elements), as we could infer from comparisons among the ten realizations we had used for each parameter set. In the applications of our method, there are always *many* lenses in each of our "lines of sight," and since we will use 100 or more different lines of sight for our statistical analyses, the deviations relative to the WN93 values will get (much) smaller, again as a result of decreasing statistical noise. Hence, we get a fair enough representation for the low and moderately high magnification regime. As we are interested mainly in global statistical properties rather than in local ones, this test shows that our approach is justified.

3. DETERMINATION OF THE UNDERLYING MATTER DISTRIBUTIONS

The matter evolution used in this paper is simulated by a Particle-Mesh (PM) N-body code (Cen 1992). But a direct, brute force calculation with such a code cannot cover the dynamic range needed; a ratio of cluster-cluster separation (100 h^{-1} Mpc) to the lensing scale of arcseconds (10 h^{-1} kpc) translates to 10^{12} mesh points, which is far beyond the capacity of the current generation of supercomputers. In order to overcome this problem, a novel scheme involving convolution of a small-scale simulation box (which provides good resolution) with a large-scale simulation box (which provides good statistical information concerning clusters) was developed by CGOT. We basically use their scheme of convolving two box sizes, but we add a few essential improvements. Our scheme is described in detail in the Appendix.

The three-dimensional matter distribution derived from these calculations is given for any cosmological time as three two-dimensional projections onto the x-y, y-z, and x-z planes, with an effective resolution of comoving 10 h^{-1} kpc, which is necessary in order to study the lens effects on small angular scales of approximately $5''$. If we wished to study still smaller scales, hydrodynamic simulations (cf. Cen 1992; Katz, Hernquist, & Weinberg 1993; Navarro, Frenk, & White 1994; Summers, Davis, & Evrard 1995; Steinmetz & Müller 1994) would be required, since the baryonic component begins to dominate over the dark matter component within 10 kpc. The essence of the convolution method is to note that small regions of given overdensity (or underdensity) act for most processes as if they were in homogeneous universes of larger (or smaller) mean density. For details and checks of the method see the Appendix.

For a typical lensing simulation, a few hundred lens planes with size $L = 5 h^{-1}$ Mpc are required. Ideally, one would like to have as many independent cosmological sequences as lens planes used. This is not achievable for reasons of limited CPU time. But neither is it really necessary; for most of the planes, only a small fraction of the matter distribution is "illuminated" by the bundle of light rays (see Fig. 1). In practice, we produced 56 independent evolutionary runs. For a given lens redshift, the particular run to be used for the particular lens plane is chosen randomly, as is the projection from among the three possible ones and the location and orientation of the square region that is "illuminated" by the rays.

The computing time for such a lensing simulation is directly proportional to the number of lens planes used.

Most of the lens planes have densities below the average density of the universe (because a few have a high overdensity), and some are almost completely empty. These lens planes contribute very little to the deflection angle. We experimented with bunching together a couple of lens planes at adjacent redshifts; this means adding up the matter distributions and treating the combined matter distribution as a single "pseudo" plane. We found that for a grouping of about 10 real lens planes into one pseudo lens plane, the results (see next sections) are indistinguishable from those obtained by treating all the lens planes individually. We concluded by running the simulations with only 60 pseudo planes (up to a redshift of $z_S = 3$), where each one represents a grouping of 10 real planes. That means, in fact, that one of our pseudo lens planes represents a rectangular parallelepiped of size $5\,h^{-1} \times 5\,h^{-1} \times 50\,h^{-1}$ Mpc^3.

4. MAGNIFICATION PATTERN AND MAGNIFICATION DISTRIBUTION

Figure 4a (Plate 1) shows a two-dimensional magnification pattern, representing the magnification as a function of source position at redshift $z_S = 3$ for one particular lensing run of our example cosmology, a standard CDM model with $\Omega = 1$ and $\sigma_8 = 1.05$. The magnification is shown as a function of position in the source plane. By definition, the average magnification is $\langle \mu \rangle = 1.0$, or $\langle \Delta m \rangle = -2.5 \log \langle \mu \rangle = 0$, i.e., equal to the case were all the matter is smoothly distributed. Whenever we use "magnification" (or demagnification) subsequently, we mean magnification (or demagnification) relative to a situation in which all matter is smoothly distributed.

The magnification as a function of position in the source plane is shown color coded in Figure 4a (Plate 1); it increases from blue through green and from red to yellow. The borderline between green and red corresponds roughly to the average magnification, $\mu = 1.0$. Green regions have magnifications slightly less than 1 (i.e., they are slightly demagnified as compared to a universe in which all matter is smoothly distributed). Red color indicates magnifications of up to 1 mag, yellow indicates magnification by more than 1 mag. Note that there is quite a large region that is demagnified by a small amount, and a few relatively small spots that are quite highly magnified.

Such a magnification pattern in the source plane is similar to the magnification patterns used in microlensing simulations at much smaller angular scales (e.g., Wambsganss, Paczyński, & Schneider 1990). One difference between the magnification patterns used here and those used in microlensing is that for microlensing, one is interested in the change of magnification as a function of time (due to the relative motions of observer, lens, and source), whereas here we only study the changes in magnification as a function of position. Another difference is that here we find caustics (and multiple images) only in rare cases, because we basically study the lens properties of a more or less smooth mass distribution; in such a situation, the surface mass density must be above the critical value in order to produce caustics. In (quasar) microlensing, ensembles of point lenses are studied, which always produce many (micro) images and, correspondingly, many caustics.

One example of a two-dimensional distribution $\mu(x)$ of magnification in the image/sky plane (cf. eq. [3]) is shown in Figure 4b (Plate 2). This shows the magnification that an image seen at this particular position in the sky would have.

The color assignment is the same as for Figure 4a (Plate 1), except that here we see locations with black color, which indicates formally very high negative values of magnification. The boundaries between regions with high positive magnifications and those with high negative magnifications (transitions from yellow to black) are easy to identify. These are the critical lines.

This image plane magnification distribution is quite similar, but not identical, to the magnification distribution in the source plane shown in Figure 4a (Plate 1). The differences are most obvious for highly magnified positions corresponding to multiple images. Whereas in Figure 4a (Plate 1) (magnification pattern in the source plane), the total magnification of all images corresponding to these source positions is displayed, in Figure 4b the sky plane magnifications of the different images at the corresponding positions are shown. From the distribution in Figure 4b (Plate 2) alone, however, it is not obvious which images belong to the same source position.

In Figure 5, the magnification probability distribution for the underlying cosmological model is shown. The top panel shows the differential distribution $f(\mu) = dn/d\ln\mu$, the bottom panel the integrated distribution $f(>\mu)$. The distribution is sampled in 20 equally spaced logarithmic intervals per decade of the magnification μ. (In contrast to most other figures, this one shows the result of all 100 different realizations, rather than for an "example" line of sight only.) In the differential distribution (top panel), there is a strong peak just to the left of magnification $\mu = 1.0$, and a power-law tail $[f(\mu) \propto \mu^{-2}]$ to high magnifications, until the probability drops to zero because of the finite resolution. This power-law behavior is a generic property of the lens equation (see, e.g., Berry & Upstill 1980). The thin solid line in Figure 5 indicates the magnification distribu-
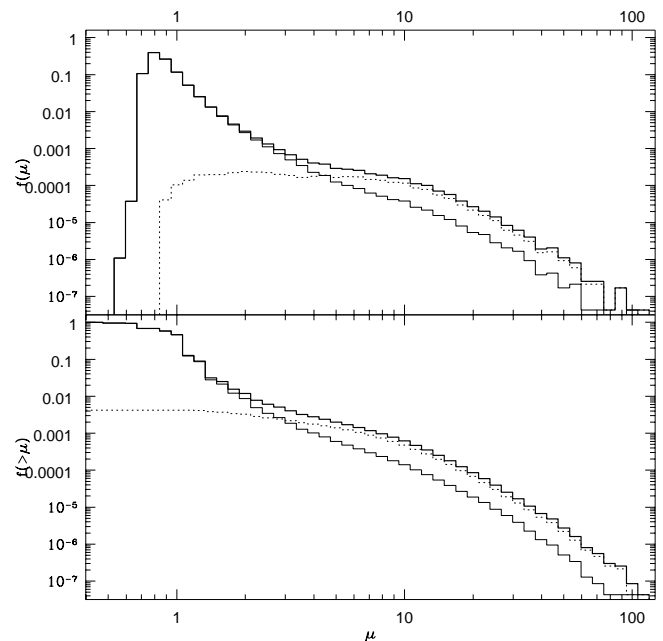

FIG. 5.—Magnification distribution from 100 different realizations (i.e., about 2.5×10^7 different source positions at a redshift of $z_S = 3.0$). *Bold line*: all source positions; *thin solid line*: singly imaged source positions only; *dashed line*: multiply imaged source positions only. Top panel shows the differential distribution $f(\mu)$, bottom panel the integrated one $f(>\mu)$. The typical (unlensed) source becomes slightly fainter, but there is a power-law tail of highly magnified sources.

tion for single image cases only, while the dotted line represents multiple images only (the bold line is the sum of the two). Because of the rareness of very high magnifications, the high-magnification end naturally is quite noisy.

The magnification distribution in Figure 5 can be interpreted as the "transfer function" of the matter in the universe (for this particular cosmological model). In other words, any intrinsic luminosity function of, say, quasars, will be folded with this magnification distribution, and what we see as the observed quasar luminosity function will be the convolution of the intrinsic luminosity function with this transfer function of the universe (Vietri & Ostriker 1983). In principle, one can determine the intrinsic quasar luminosity function for a given cosmological model once the observed luminosity function and the transfer function of this cosmological model are known (Ostriker & Vietri 1986). In practice this will turn out to be nontrivial, mainly because the observed luminosity function of quasars is not well known (Boyle, Shanks, & Peterson 1988).

The effect of this transfer function is even more obvious when it is applied to a population of perfect standard candles at high redshift; for a given source redshift, the luminosity function (originally a delta function in such a case) will be broadened to exactly the shape $f(\mu)$ indicated by the curve in the top part of Figure 5. The slope of this magnification probability function for gravitational lensing is known analytically in the limit of very high magnifications (TOG; Schneider 1987; Blandford & Narayan 1986) and should therefore be independent of the cosmological model. However, in the intermediate range from small to moderate magnifications, different cosmological models produce different magnification probability distributions.

5. CAUSTICS, CRITICAL LINES, AND MULTIPLE IMAGES

As described in § 2, the positions of all rays in the image plane and source plane are stored for each lensing run.

Therefore, it is straightforward to determine characteristics of the mapping $y = Ax$ between the positions in the image plane x and those in the source plane y (see SEF, Ch. 5).

Of particular interest are the points in the image plane x at which the Jacobian determinant det $A(x)$ changes its sign (these points can be seen in Fig. 4b [Pl. 2] as locations where the color changes from yellow to black). By definition, these are the *critical lines*. In Figure 6a the critical lines are plotted for this particular line of sight. Mapping these critical lines onto the source plane results in the *caustics*. These are shown in Figure 6b. Comparing Figure 6a and 6b, it is not too difficult to find out which caustic belongs to which critical line.

The shapes of the critical lines and of the caustics found in these lensing simulations are quite irregular; they are certainly different from the symmetric shapes that are obtained for simple models of lenses, e.g., singular isothermal sphere plus external shear or elliptic potential (e.g., Blandford & Kochanek 1987; Kormann, Schneider, & Bartelmann 1994). The reason is simply that the mass distributions we use are not at all symmetric, but rather represent the irregular real distribution of matter in the universe.

Whenever the source position is inside such a closed caustics line, a pair of new (usually highly magnified) images emerges. When the source is outside, but near, a caustic, one highly magnified image results. In Figure 7, various image configurations are shown that are produced by the caustic structure in the top right of Figures 4a and 6b. These indicate the variety of image shapes and morphologies that are produced by this particular caustic structure, ranging from a very stretched (and highly magnified) single image at the top left through elongated and aligned double and triple images of similar magnification, to cases with faint central (radial) images. For comparison, the shape and size of an unlensed source is indicated at the bottom right corner of the bottom right panel.
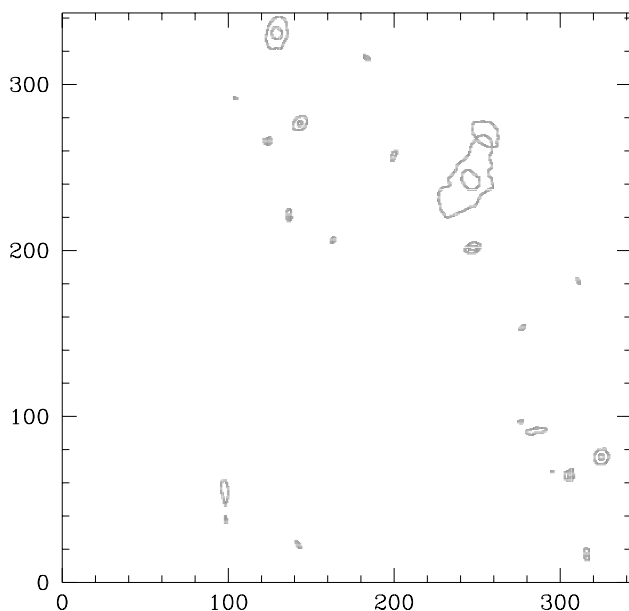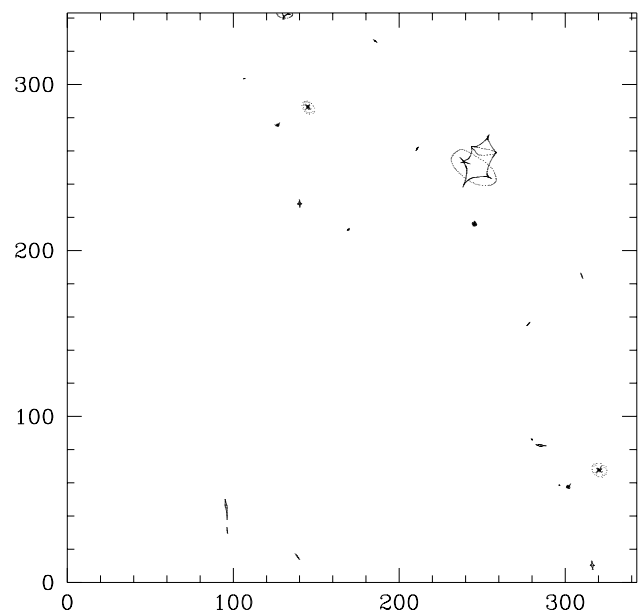

FIG. 6a

FIG. 6b

FIG. 6.—(a) Critical lines in the image plane and (b) caustics in the source plane for our example line of sight are displayed, for a source redshift of $z_S = 3.0$. The critical lines are the locations at which the determinant of the Jacobian matrix disappears; the caustics are these points mapped onto the source plane (cf. Figs. 4b and 4a, respectively). Scale is in arcseconds.
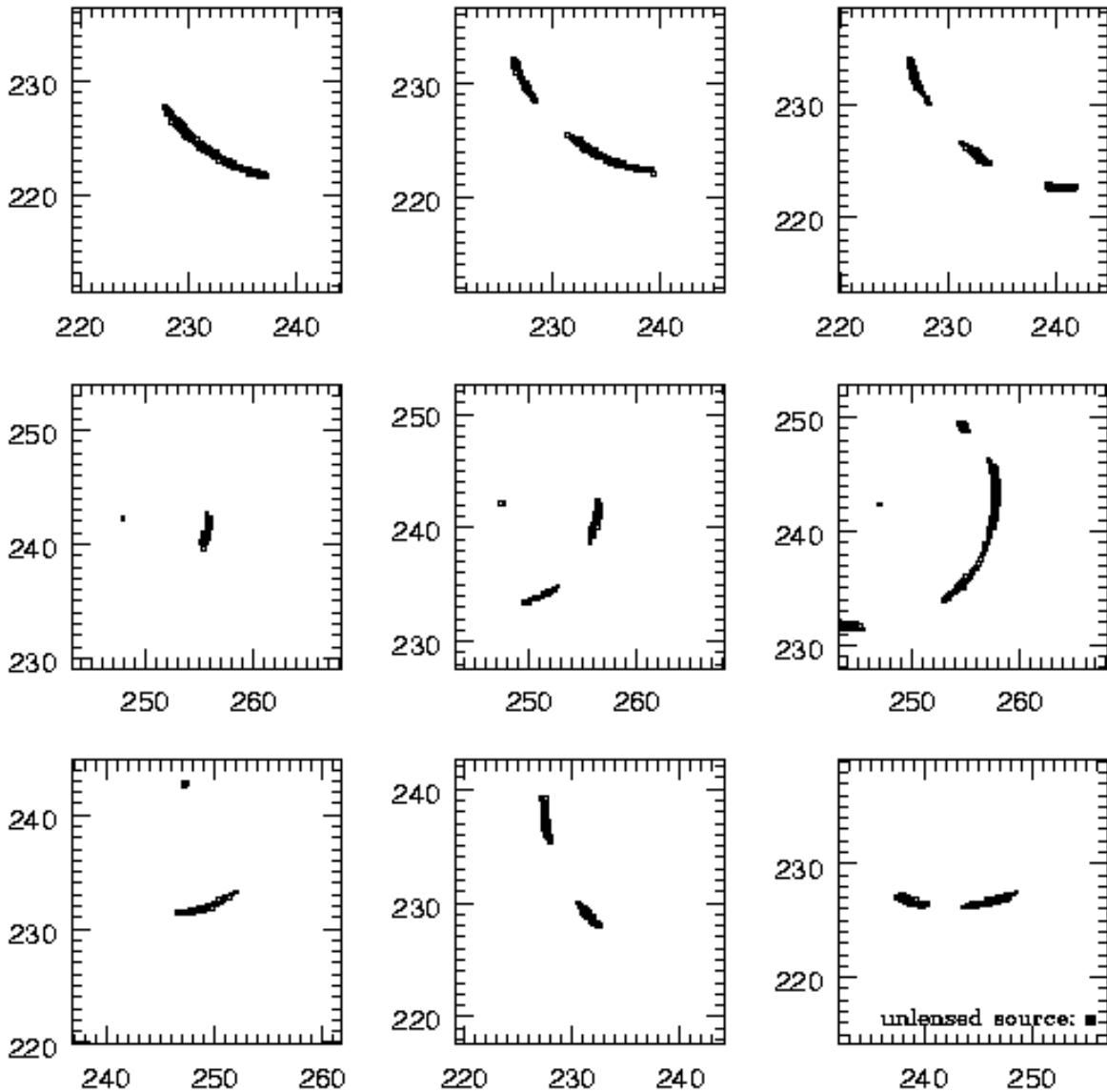
FIG. 7.—Various image configurations with large magnifications, showing the range of possible geometrical arrangements of images. In the bottom right part of the bottom right panel, the size and shape of the unlensed source is indicated (relative scale in arcseconds).

One can look at these image configurations from two different viewpoints. If the source is extended (e.g., a distant galaxy), then Figure 7 shows the highly extended images that could be observed: giant arcs, arclets, and tangentially aligned images. On the other hand, if the source is an unresolved quasar, then the area of the images reflects the magnification of the two or more quasars that are seen. The separation between the centers of light would be the distance between the multiple images.

6. GIANT ARCS, ARCLETS, TANGENTIALLY ALIGNED GALAXIES, AND SHEAR MAPS

In this section, we show the effects of gravitational lensing due to our three-dimensional ray tracing on various ensembles of sources. In the left column of Figure 8, we show four different fields of sources: a regular grid of circular sources, randomly distributed circular sources, a regular grid of elliptical sources (with fixed ellipticity and random position angle), and randomly distributed elliptical sources with fixed ellipticity. The diameter of the circular sources shown here is about 3″. At the corresponding right-hand side, the

resulting image configurations are shown; this is what a telescope would see if a galaxy distribution at redshift $z_S = 1$ such as that on the left side were seen through the matter distribution in front of it. The size of an image reflects the magnification, since surface brightness is conserved by gravitational lensing; the area of the images divided by the area of the corresponding source is the magnification of this particular image. Since all source sizes and shapes are identical in one panel, the relative areas of the images reflect the relative magnifications. In panels with a regular grid of source positions, it is very obvious from the deviations of the chains of galaxies from straight lines where the largest matter concentrations exist along the line of sight (cf. the map of the matter in Figure 3b).

Since all the sources have identical intrinsic sizes and shapes in each panel (circular or constant ellipticity), each deviation from that shape on the right-hand side is lens induced. One can see a large variety of distorted image shapes: slight ellipses from circular sources, small arcs, "straight arcs," giant arcs, big blobs, and more complicated image structures. Perhaps most obvious is the tendency to
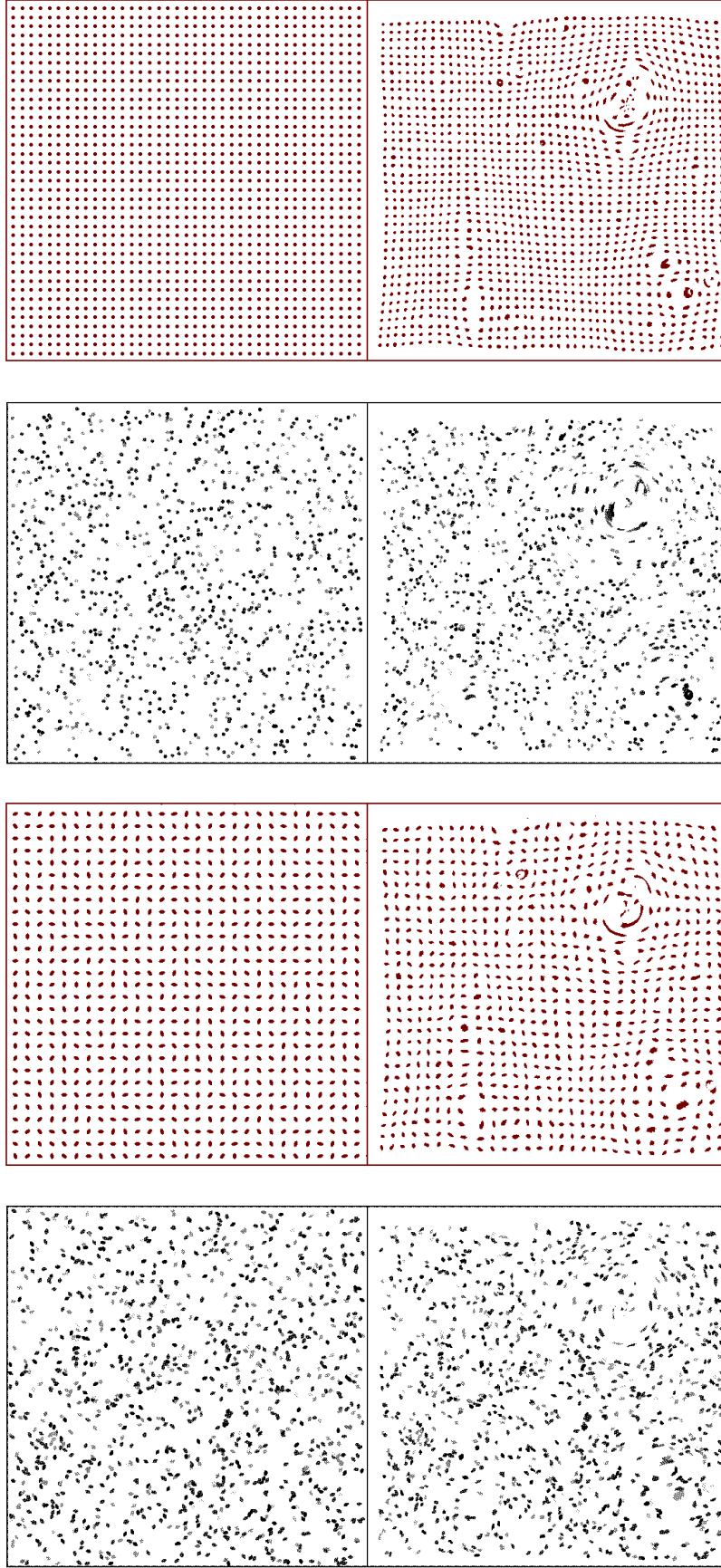
FIG. 8.—Various distributions of sources at redshift $z_S = 1.0$ and corresponding images as seen through the three-dimensional matter distribution, i.e., weakly and strongly lensed sources. The source configurations are to the left, image configurations to the right. From top to bottom, the source ensembles are: circular sources in a regular grid and randomly distributed, elliptical sources (random orientation) in a regular grid and randomly placed. The source sizes are about $3''$. The source density is equivalent to about 40,000 galaxies per deg^2. Panels are about $343''$ at a side.
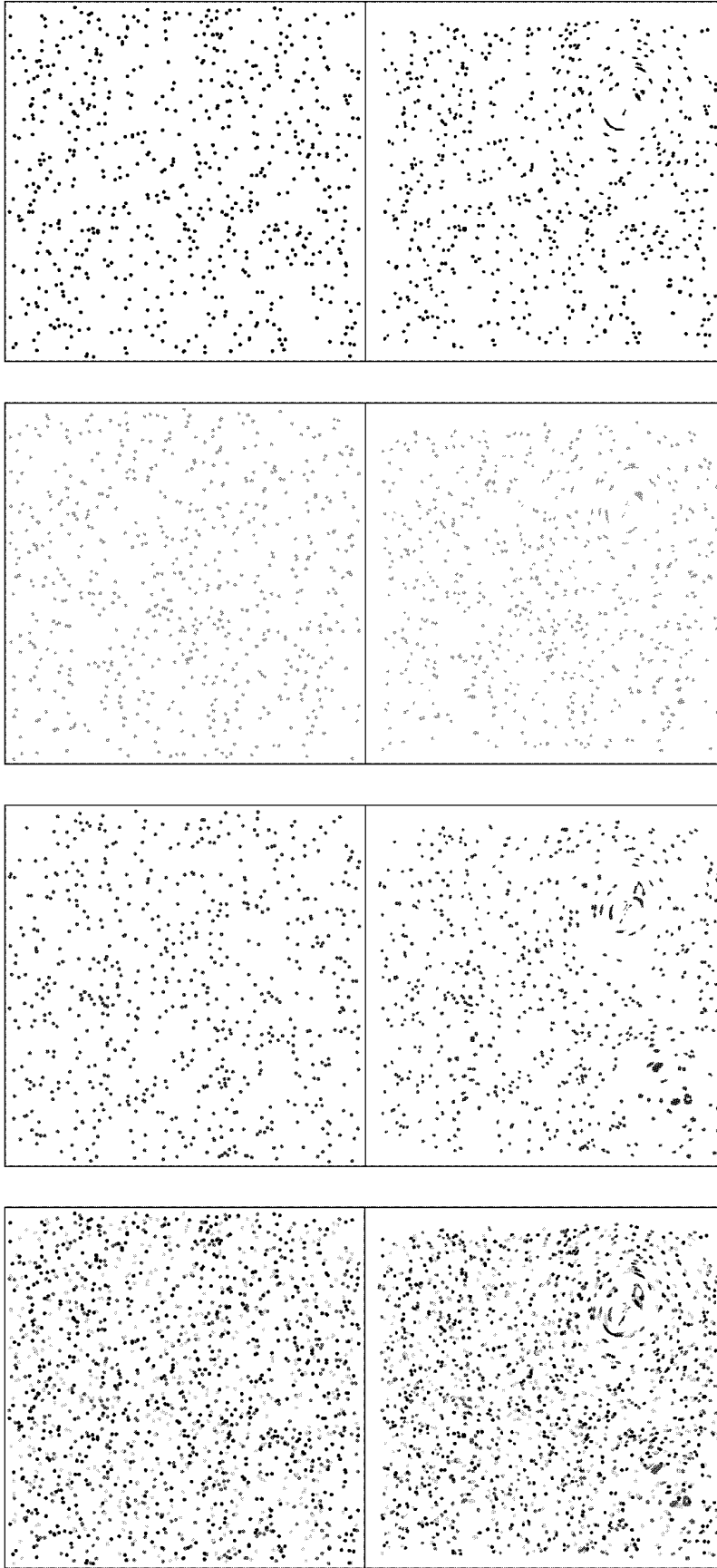
FIG. 9.—As Fig. 8, but here source planes (*left*) and image planes (*right*) are shown for three different source redshifts: from top, $z_S = 1$, $z_S = 2$, $z_S = 3$. Bottom row shows superposition of the three source redshifts.

41

"tangentially aligned" (roughly) elliptical images, whose major axes are approximately perpendicular to the radius vector from the center of the mass concentration.

In Figure 9, the lensing effect of our example line of sight is shown for three different source redshifts: left columns from top to bottom show three sets of circular sources with random positions at source redshifts $z_S = 1$, 2, and 3. The second column shows the respective image configurations that one would see in the sky through the deflecting matter between source plane and observer. In the bottom row, the three source populations are superimposed, with the different redshifts indicated by three different gray scales.

In § 2 we described how to obtain the surface mass density κ (cf. eq. [4]) along the line of sight, as measured by the light rays. In Figure 4c (Plate 3) we show the distribution of the effective surface mass density κ for our example field of view. The highest density clumps are easily identifiable with the highest magnification regions in Figures 4a and 4b (Plates 1 and 2). It is also quite obvious that the magnification $\mu(x)$ (Figure 4b) follows the surface mass density distribution very closely (Figure 4c) in the low-magnification regime. This indicates that the convergence, the matter inside the beam, is mainly responsible for the magnification, and less so the shear field from outside the beam.

For each of our artificial lines of sight, we can obtain the distribution of the shear fields as shown in equations (5a) and (5b) (see § 2). For our example line of sight, this shear distribution $\gamma(x)$ is shown for a source redshift of $z_S = 1.0$ in Figure 4d (Plate 4). The length of the straight lines is proportional to the absolute value of the shear, and the direction represents the direction of the shear. It is quite obvious that the big lump of matter at the top right produces the strongest shear; the lines clearly indicate the tangential alignment expected for galaxies that are behind such a cluster of galaxies. Similar shear distributions have recently been obtained observationally by various groups studying the distribution of shear in fields around rich clusters of galaxies (e.g., Bonnet et al. 1993) or in "empty" fields (Mould et al. 1994). Observationally, the shear fields are obtained by averaging the ellipticities of galaxies in small fields of a few tens of arcseconds. The idea is that this averaging should cancel the intrinsic distribution of position angles, and as a net effect should show only the effective shear produced by the gravitational lens effect of the foreground matter.

7. SUMMARY AND OUTLOOK

We have presented a method for determining the lensing properties of a three-dimensional, fully nonlinear distribution of matter obtained from cosmological simulations. We explain the techniques used to calculate the light deflection by a large number of lenses in many lens planes. The simulations produce maps of the magnification in the source and image plane. We study the caustics and critical lines for each matter realization individually, or in a statistical way for a large number of realizations. Here, one particular "line of sight" with a matter distribution from a standard CDM model with $\Omega = 1$ and $\sigma_8 = 1.05$ is used to illustrate the diagnostic power of the applications. It is straightforward to apply this method to other cosmological models, and we plan to do so with significantly higher resolutions in both cosmological simulations and ray-tracing methods. There are numerous possible applications of this ray shooting technique. Just to mention a few (some of them already being pursued):

1. Study of frequency, geometry, magnification ratio, and separation of multiple images. What fraction of quasars is multiply imaged? How many double, triple, or quadruple images do we obtain (for given observational limits of spatial resolution and dynamic range)?

2. Study of the distribution of magnification of certain classes of objects (galaxies, quasars). This can be done separately for single and multiple image cases, or for both combined, addressing question such as: are there many highly magnified quasars that are single (rather than multiply imaged)? One straightforward application, the quantitative study of the dispersion effect of lensing on standard candles at moderate redshifts (i.e., on supernovae of Type 1), has already been published (Wambsganss et al. 1997).

3. Study of correlations between single or multiple quasars and strong ("visible") mass concentrations at or near the line of sight (which may affect the issues of dark lenses and/or quasar-galaxy associations).

4. Study of the effects of chance alignments of dense matter clumps along the line of sight. How accurate are mass determinations that assume that all matter responsible for the lensing is in a single plane?

5. Study of the shear distribution or tangentially aligned galaxies around (rich) clusters and in "empty" fields. What is the average or rms shear value in random lines of sight?

6. Use of techniques for reconstructing mass profiles of galaxy clusters from weak lensing (Kaiser & Squires 1993) and comparing the reconstructed mass profile with the actual one. Are there any systematic effects due to foreground and background matter?

7. Comparison of frequency and properties of arcs and "straight arcs" produced by extreme lensing in clusters with those seen in the real world.

8. Study of the effects of three-dimensional lensing on the cosmic microwave background.

Most of the points above will be investigated for sources at different redshifts. The expected and computable gravitational lensing properties of the different models that have been proposed for the growth of structure in the universe will vary greatly from model to model. Thus, a quantitative comparison between observed and expected lensing properties should offer great advantages in selecting among the competing models, and ideally allow us to eliminate models that fail to correspond to reality. Even at present, the strongest constraints on the size of the cosmological constant are derived from lensing statistics (Fukugita & Turner 1991; Kochanek 1992, 1995; Maoz & Rix 1993). In a recent application of the method described here, we found that the standard CDM model predicts far more large splitting multiple quasars than are observed (Wambsganss et al. 1995). It will be very interesting to see if other models, such as mixed dark matter, CDM + Λ, or open models, can survive this gravitational lensing test.

APPENDIX A

DESCRIPTION OF THE CONVOLUTION TECHNIQUE

Here we describe the convolution method that is used to compensate for the lack of sufficient spatial dynamic range in the N-body simulations. As stated earlier in the main body of this paper, for gravitational lensing applications, one must have enough scale-resolving power to reach scales that are interesting and accessible to observations ($\sim$ arcsecond). But it is not possible at the same time, in a single simulation, to reach the other end of the spectrum, the large-scale waves of the universe, in order to obtain a fair sample of the relevant cosmic systems, which in this case are clusters of galaxies. A minimal desired dynamic range will be a few times the ratio of cluster separation ($\sim 50\ h^{-1}$ Mpc) to cluster core size ($50\ h^{-1}$ kpc), i.e., a few thousand, which was not achievable at the time the simulations used in this paper were computed.

As an alternative to the brute force approach, we made two kinds of simulations: one with box size $L = 5\ h^{-1}$ Mpc (hereafter Box S) and resolution of $10\ h^{-1}$ kpc, the other with box size $L = 400\ h^{-1}$ Mpc (hereafter Box L) and resolution $0.8\ h^{-1}$ Mpc (both simulations use $500 \times 500 \times 500$ cells with a PM N-body code). In computations of both boxes (S and L), we assume periodic boundary conditions. That is, we assume that both boxes have the same mean density as the universe at any given redshift. For the large box this is a good approximation, since the amplitudes of waves on scales larger than $400\ h^{-1}$ Mpc are quite small at $z = 0$ and even smaller at the redshifts relevant for lensing. But for the small box, this assumption is poor. The nonlinear scale at $z = 0$ is approximately $8\ h^{-1}$ Mpc, so in the L box we will find $5\ h^{-1}$ Mpc subboxes at a variety of over- and underdensities. Then, using this distribution, we convolve Box S (which has small-scale resolution) with Box L (which has large-scale power), details of which are described below. In Table 1 we present the parameters of the two types of simulations performed.

We also note that at the time this paper was being written, we were using new N-body techniques to make simulations that can cover this needed range directly. We note that the gravitational ray-tracing method presented in the paper is independent of the convolution method described here.

Before a step by step description of the convolution method, it is useful to define a few quantities. The actual over- or underdensity of a particular plane, $R = \Sigma/\langle\Sigma\rangle$, drawn from the density distribution $f(R)$ on the scale of Box S $(5\ h^{-1}$ Mpc$)^3$, which is computed from Box L (containing 512, 000 subboxes, each of which is a $[5\ h^{-1}$ Mpc$]^3$ cube). R is the ratio of the density in Box S to the mean cosmic density. The projection of the matter in a Box S onto one of the three orthogonal planes makes a surface mass density screen, $\Sigma_1(x)$. We now detail steps to do the convolution.

1. We first choose R randomly from $f(R)$.
2. Then a mosaic square region, $\Sigma_2(x)$, consisting of $N^2\Sigma_1(x)$ screens, where $N = 2, 3, 4\ldots$, is set up. The number of repetition screens, N, in each dimension on the projection plane is determined by R such that the shrunken $\Sigma_4(x)$ (when $R > 1$, see step 4 below) still has a comoving length larger than $1.5 \times (5\ h^{-1}$ Mpc$)$, to prevent situations of no defined densities, when rays shoot outside the original region.
3. From Σ_2 we obtain a new screen, $\Sigma_3(x)$, equal to $\Sigma_2^{R^{0.07}}(x)$, where the power operation operates on each individual cell of screen Σ_2. This step is designed to mimic the evolution of regions with different densities, and the value 0.07 is empirically determined using simulations. This step does not, to first order, change the overall density, but it increases the contrast (for $R > 1$). Since $R^{0.07}$ is always very close to unity, this step affects the results very mildly.
4. Next, we rescale each of the two dimensions of the screen $\Sigma_3(x)$ by $R^{-1/3}$. This involves resampling the surface mass onto a smaller (or larger) grid for $R > 1$ ($R < 1$), increasing (or decreasing) the surface density by $R^{2/3}$, resulting in a new screen, $\Sigma_4(x) = \mathrm{SCALE}(\Sigma_3(x))$. This step is to take into account the fact that high-density regions should have been compressed to smaller comoving regions during their evolution.
5. The density in each of the new pixels of Σ_4 is multiplied by $R^{1/3}$, to account for the fact that the line-of-sight dimension is also reduced, yielding $\Sigma_5 = R^{1/3}\Sigma_4$.
6. We then randomly choose an origin and randomly rotate screen Σ_5 to get, by bilinear interpolation, a new screen Σ_6 with the original comoving pixel size ($10\ h^{-1}$ kpc).
7. Finally, we renormalize Σ_6 such that $\langle\Sigma_6\rangle = R \times \langle\Sigma_1\rangle$, which will be the end product of this scheme. The renormalization factor R is typically close to unity.

Figure 10 illustrates this convolution. The four panels correspond, respectively, to the original surface mass density distribution Σ_1 (*top left*), a part of the shrunken or expanded distribution Σ_5 (*top right*), the full Σ_5 (*bottom left*), and the final

TABLE 1

PARAMETERS OF THE N-BODY SIMULATIONS

N_{sim}	L (h^{-1} Mpc^{-1})	Δl (h^{-1} kpc^{-1})	N_{cell}	N_{part}
56......	5.0	10.0	500^3	250^3
1......	400.0	800.0	500^3	250^3

NOTE—N_{sim}: number of simulations of this kind; L: side length of the simulation box; Δl: distance between two grid points; N_{cell}: number of resolution cells; N_{part}: number of particles.

rotated and normalized distribution Σ_6 (*bottom right*). Figure 10a shows this for a factor of $R = 1.6$ (overdense), and Figure 10b for $R = 0.625$ (underdense).

This convolution method is tested against a high-resolution P^{3}M simulation (E. Bertschinger 1995, private communication), where the box size is 100 h^{-1} Mpc and therefore contains large-scale power. Of course, this P^{3}M simulation does not reach the resolution of 10 h^{-1} kpc at the small scale end, so we can only make comparisons in the overlapping region. Figure 11 shows the (normalized) surface mass density distributions on a cell of area $125 \times 125\ h^{-2}$ kpc^2 with a depth
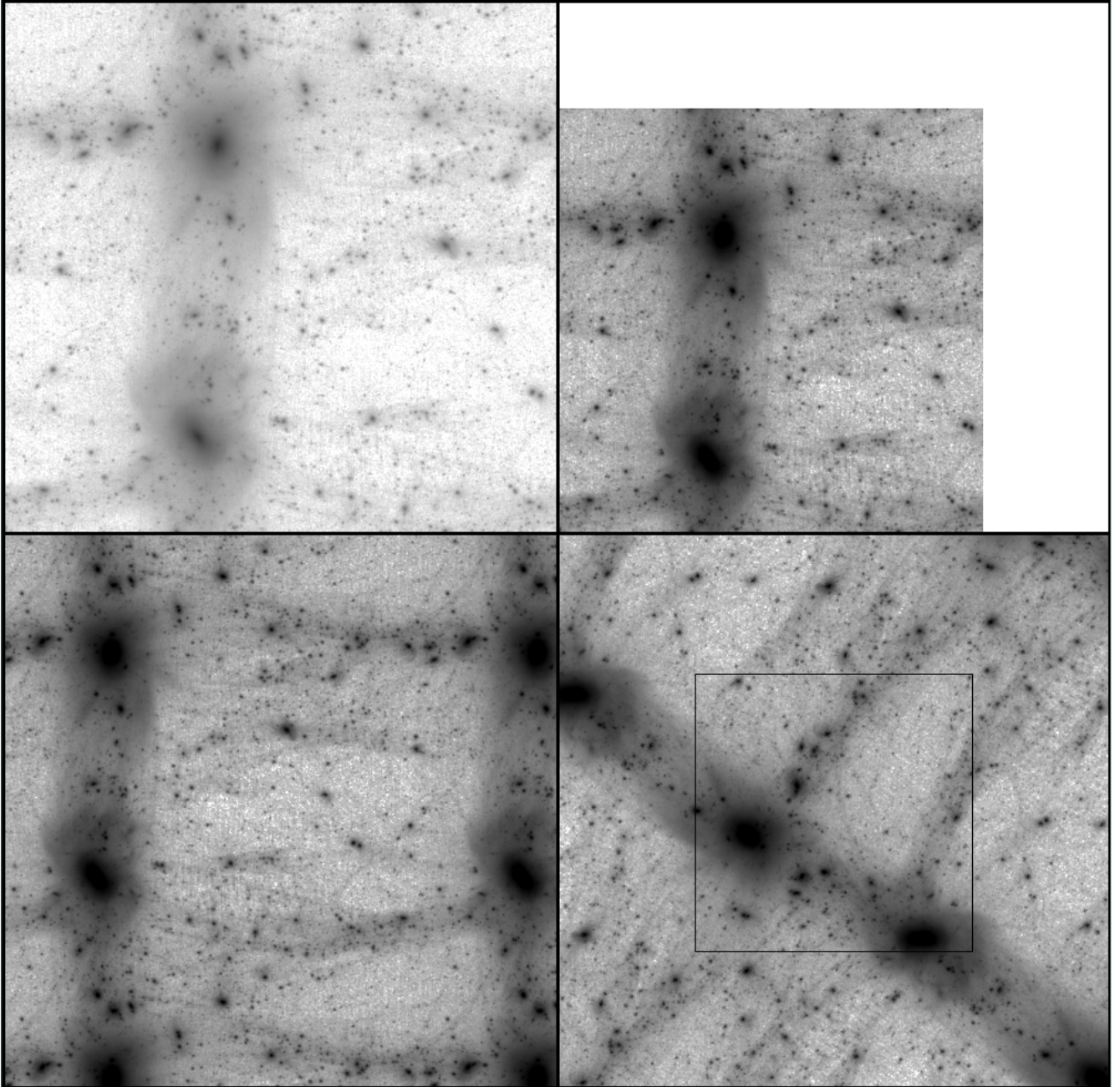
FIG. 10a

FIG. 10.—The panels in this figure illustrate the convolution technique described in the Appendix. In (a), the top left panel represents the matter distribution Σ_1 in one of the 5 h^{-1} Mpc cubes with average density at redshift $z_L = 0.73$. Here, this particular plane should represent a randomly determined overdensity of 1.6 (a larger than typical case chosen for purpose of illustration); therefore, the matter is contracted in the x- and y-direction each by $(1.6)^{1/3}$, and multiplied by $(1.6)^{1/3}$ (corresponding to a compression in z-direction). The resulting matter distribution is displayed in the top right panel (part of Σ_5, using the notation of the Appendix). The matter distribution is then extended in the "empty" parts of the square, taking advantage of the periodic boundary conditions (*lower left panel*, full Σ_5). This distribution is shifted in the x- and y-directions and rotated by arbitrary amounts, so that finally the lower right panel is obtained (Σ_6). The apparent doubling of the two dense matter clumps is of no concern, since the bundle of light rays with fixed angular size cuts out only a small square (as indicated in the final panel), so that no repeated structures appear in the "illuminated field." In (b), the same is shown for a (under-) density of $R = 1.6^{-1} = 0.625$.
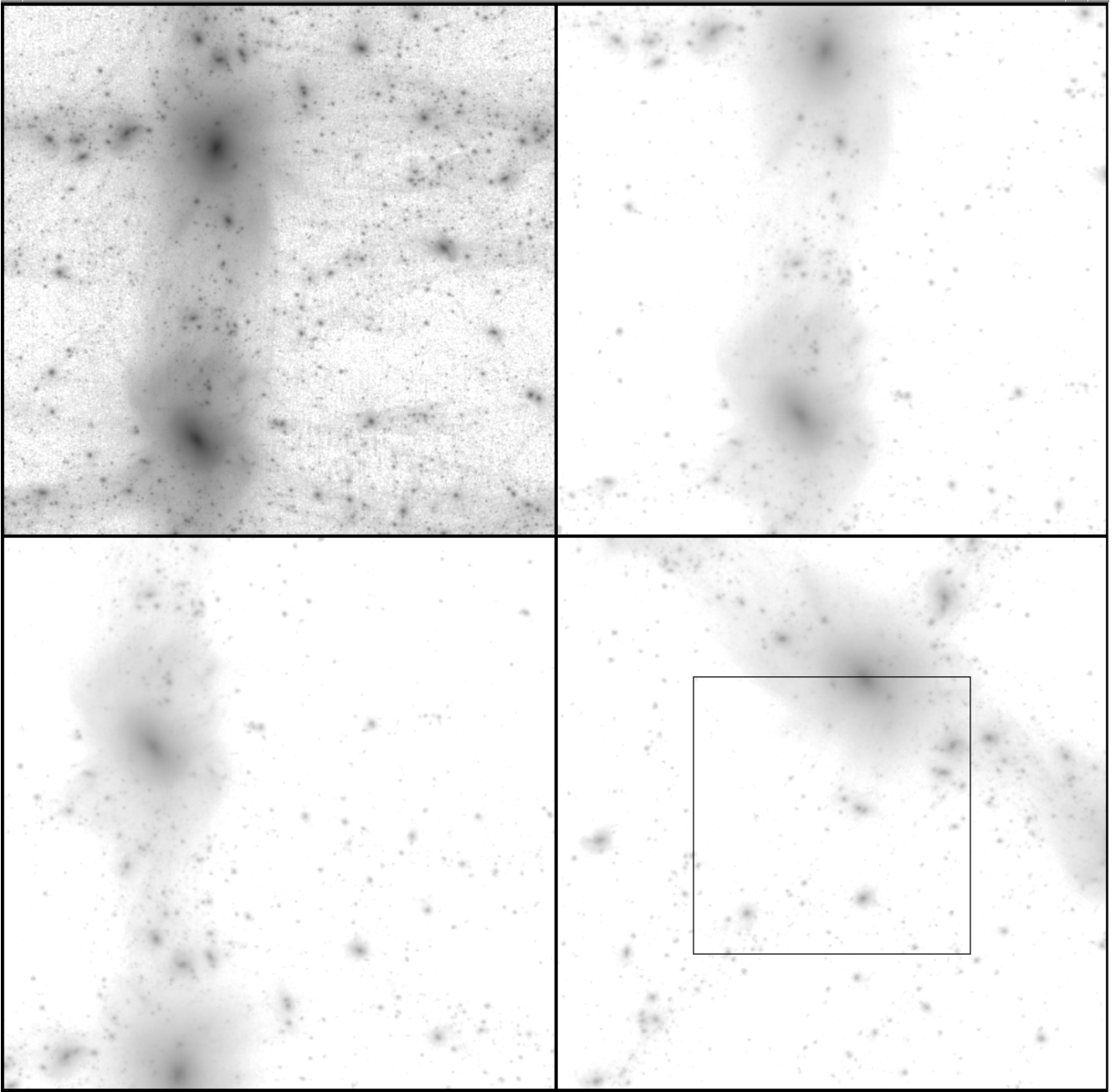
FIG. 10b

of 100 h^{-1} Mpc using our convolution method (*solid histogram*) and from direct calculation using Bertschinger's simulation (*dotted histogram*). The diagram shows the highly skewed distributions of the surface mass densities: a small fraction of these "mass cylinders" is highly overdense, about 20% have surface mass densities above average, and the majority (80%) is slightly underdense. The agreement between the high-resolution (Bertschinger) simulation and our convolved simulation is satisfactory.
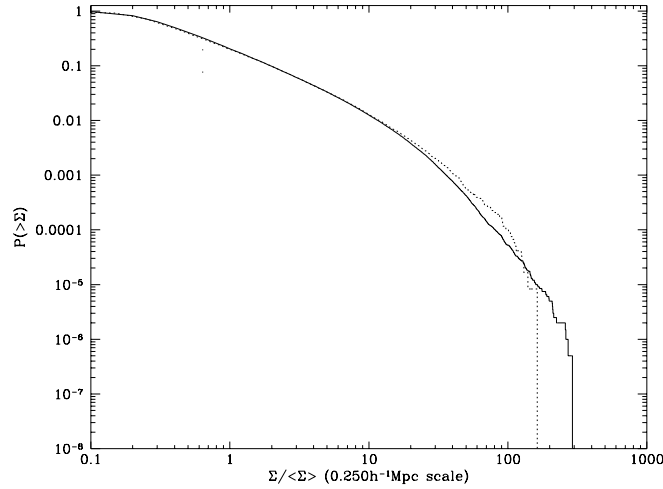
Fig. 11.—Comparison of surface mass density distributions in 125 h^{-1} kpc $\times 125$ h^{-1} kpc $\times 100$ h^{-1} Mpc cylinders using the convolution technique (*solid histogram*; see Appendix) and a direct simulation (*dotted histogram*; E. Bertschinger 1995, private communication). It indicates that the convolution method gives results that are in satisfactory agreement with direct simulations, where comparisons can be made.

REFERENCES

Babul, A., & Lee, M. H. 1991, MNRAS, 250, 407
Bartelmann, M., & Schneider, P. 1991, A&A, 248, 353
Berry, M. V., & Upstill, C. 1980, Prog. Opt., 18, 257
Blandford, R. D., & Kochanek, C. S. 1987, ApJ, 321, 658
Blandford, R. D., & Narayan, R. 1986, ApJ, 310, 568
Bonnet, H., Fort, B., Kneib, J.-P., Mellier, Y., & Soucail, G. 1993, A&A, 280, L7
Boyle, B. J., Shanks, T., & Peterson, B. A. 1988, in ASP Conf. Ser. 2, Proceedings of a Workshop on Optical Surveys for Quasars, ed. P. Osmer et al. (San Francisco: ASP), 1
Cen, R. 1992, ApJS, 78, 341
Cen, R., Gott, J. R., III, Ostriker, J. P., & Turner, E. L. 1994, ApJ, 423, 1 (CGOT)
Fukugita, M., & Turner, E. L. 1991, MNRAS, 253, 99
Górski, K. M., et al. 1994, ApJ 430, L89
Hinshaw, G., & Krauss, L. M. 1987, ApJ 320, 468
Jaroszyński, M. 1989, Acta Astr., 39, 301
———. 1991, MNRAS, 249, 430
Jaroszyński, M., Park, C., Paczynski, B., & Gott, J. R. 1990, ApJ, 365, 22
Kaiser, N., & Squires, G. 1993, ApJ, 404, 441
Kassiola, A., & Kovner, I. 1993, ApJ, 417, 450
Katz, N., Hernquist, L., & Weinberg, D. H. 1993, ApJ, 399, L109
Kochanek, C. S. 1992, ApJ, 384, 1
———. 1995, ApJ, 453, 545
Kochanek, C. S., & Apostolakis, J. 1988, MNRAS, 235, 1073
Kochanek, C. S., & Blandford, R. D. 1987, ApJ, 321, 676
Kormann, R., Schneider, P., & Bartelmann, M. 1994, A&A, 284, 285
Kovner, I. 1987a, ApJ, 321, 686

Kovner, I. 1987b, Nature, 325, 507
Lee, M. H., & Paczyński, B. 1990, ApJ, 357, 32
Maoz, D., & Rix, H.-W. 1993, ApJ, 416, 425
Mould, J., Blandford, R., Villumsen, J., Brainerd, T., & Smail, I. 1994, ApJ, 271, 31
Narayan, R., & White, S. D. M. 1987, MNRAS, 231, 97p
Navarro, J. F., Frenk, C., & White, S. D. M. 1994, MNRAS, 267, L1
Ostriker, J. P., & Vietri, M. 1986, ApJ, 300, 68
Park, C. B., & Gott, J. R., III. 1991, MNRAS, 249, 288
Rauch, K. P. 1991, ApJ, 374, 83
Schneider, P. 1987, A&A, 183, 189
Schneider, P., Ehlers, J., & Falco, E. E. 1992, Gravitational Lensing (Berlin: Springer) (SEF)
Schneider, P., & Weiss, A. 1988a, ApJ, 327, 526
———. 1988b, ApJ, 330, 1
Smoot, G. F., et al. 1992, ApJ, 396, L1
Steinmetz, M., & Müller, E. 1994, A&A, 281, 97
Summers, F., Davis, M., & Evrard, A. 1995, ApJ, 454, 1
Turner, E. L., Ostriker, J. P., & Gott, J. R., III. 1984, ApJ, 284, 1 (TOG)
Vietri, M., & Ostriker, J. P. 1983, ApJ, 267, 488
Wallington, S., & Narayan, R. 1993, ApJ, 403, 517 (WN93)
Wambsganss, J. 1990, Ph.D. thesis, Munich University (MPA Rep. No. 550)
Wambsganss, J., Cen, R., Ostriker, J. P., & Turner, E. L. 1995, Science, 268, 274
Wambsganss, J., Cen, R., Xu, G., & Ostriker, J. P. 1997, ApJ, 475, L81
Wambsganss, J., Paczyński, B., & Schneider, P. 1990, ApJ, 358, L33
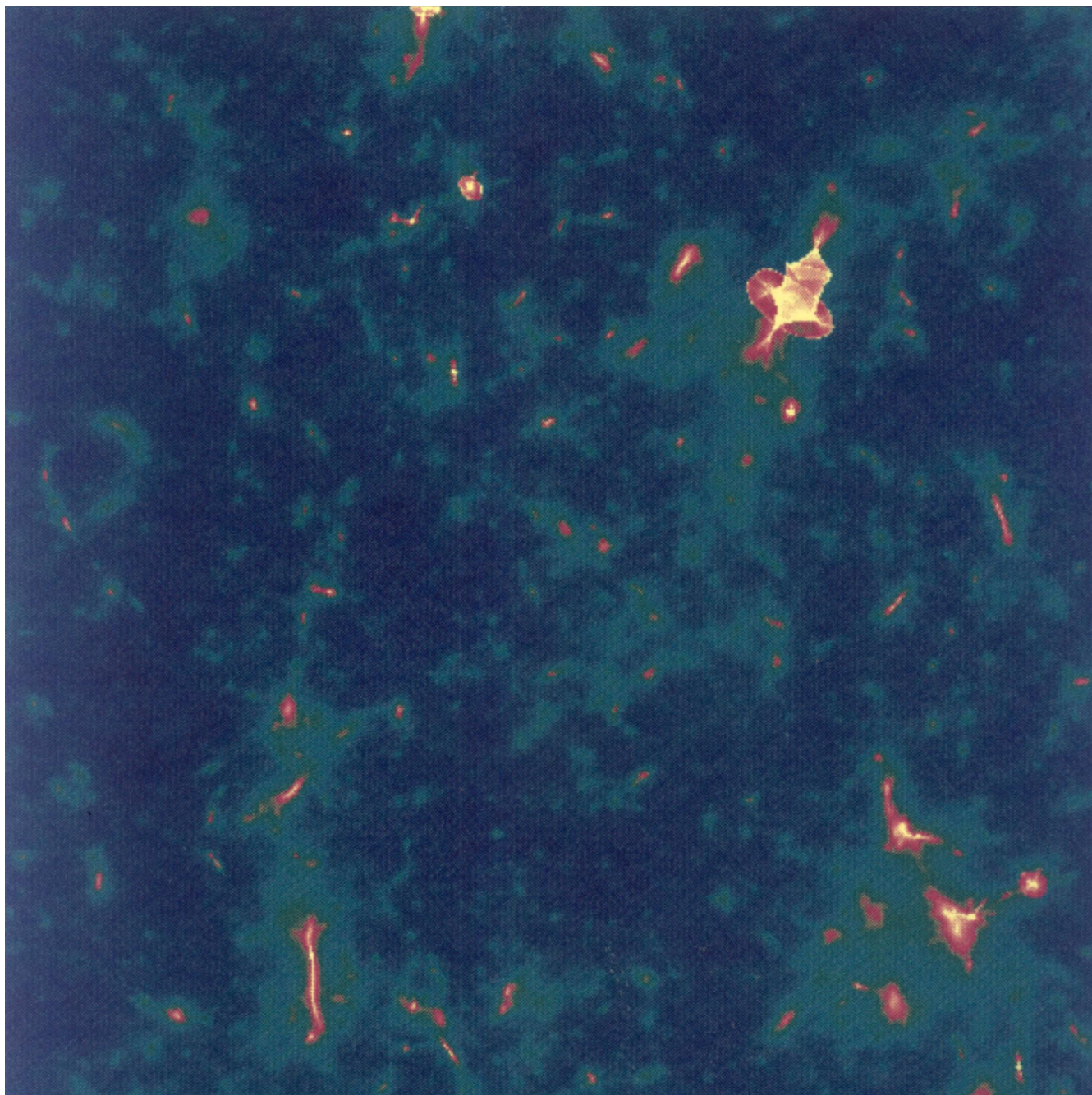
FIG. 4a.—Magnification pattern of one particular line of sight through the universe (the same as portrayed in Fig. 3). This is a two-dimensional map of the magnification as a function of position in the source plane at $z_S = 3$. The color indicates the *total* magnification of all images for a particular source position, increasing from blue through green and red to yellow. The transition between green and red marks roughly the average magnification. For the strong lens in the top right part the caustics are identifiable as sharp yellow lines, indicating very high magnification. The sidelength of this and all the other maps is 343″.
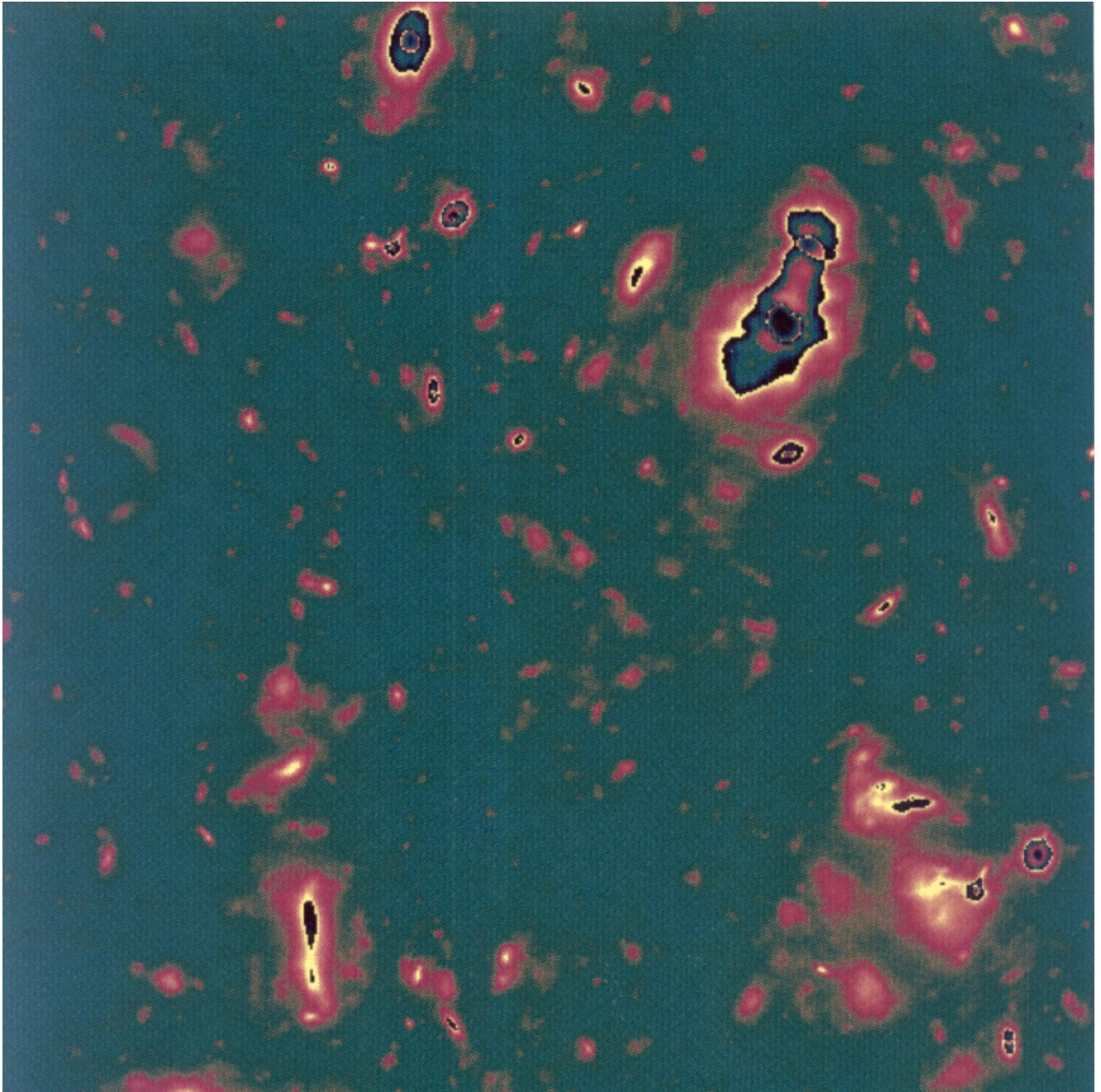
WAMBSGANSS, CEN, & OSTRIKER (see 494, 37)

PLATE 1

Fig. 4b—Magnification map in the image/sky plane. Here, the magnification of each image appearing at a certain position in the sky is indicated. The low and intermediate magnification regions are very similar to those in the map shown in Fig. 4a. At the high magnification end there are obvious differences; here, each image of a multiply imaged source would appear at a different position. Note the transitions from bright yellow to black, where the magnification changes from very high positive values to (formally) very high negative values. This boundary marks the critical lines that separate multiple images with positive and negative parity.
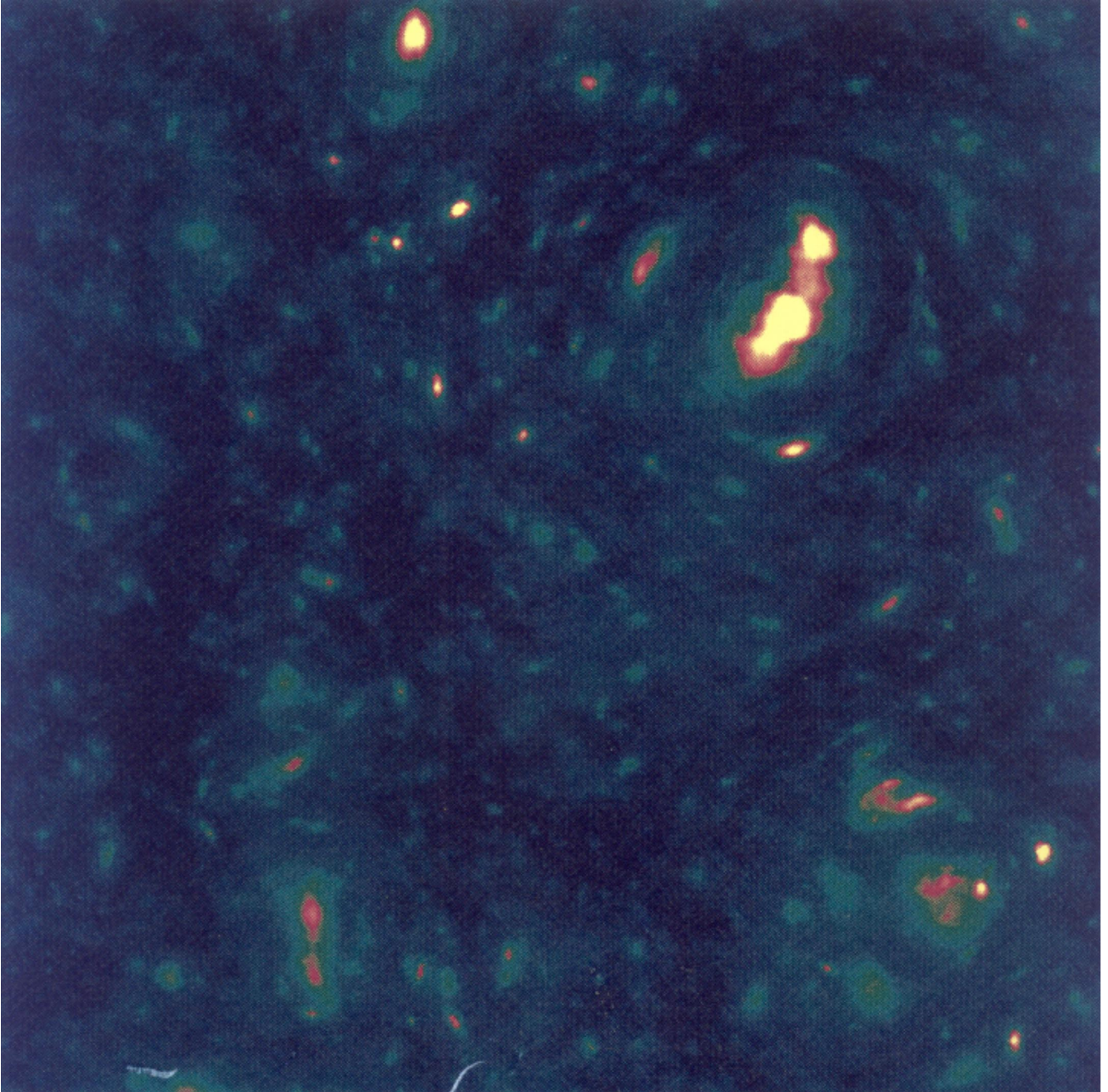
PLATE 2

Fig. 4c—Map of effective surface mass density κ or convergence along the line of sight. This distribution is quite similar to the matter integrated along the line of sight, as shown in Fig. 3b. However, here the matter is weighted by the angular diameter distances.
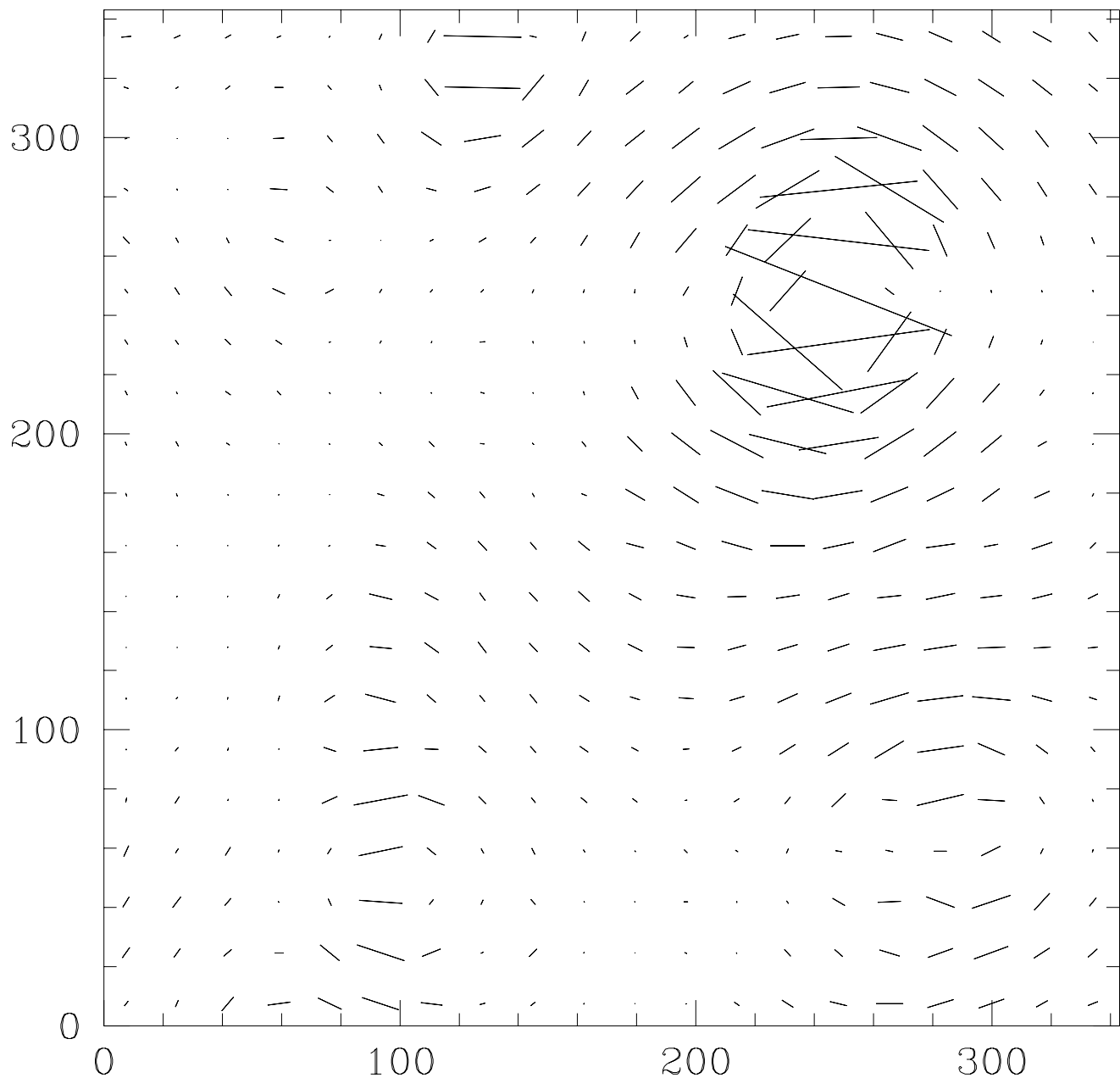
PLATE 3

FIG. 4d—Shear map for a source plane at $z_S = 1$, resulting from the foreground mass distribution in the field of view. The length of the lines indicates the relative strength of the shear; angles of the lines show the direction of the shear. The regions of strong shear are easily recognized as those with the highest mass concentrations (cf. Figs. 3b, 4a, 4b, and 4c).

WAMBSGANSS, CEN, & OSTRIKER (see 494, 42)

PLATE 4